# Quantum shot noise in mesoscopic superconductor-semiconductor heterostructures

INAUGURALDISSERTATION

zur
Erlangung der Würde eines Doktors der Philosophie
vorgelegt der
Philosophisch-Naturwissenschaftlichen Fakultät
der Universität Basel
von

Bong-Ryoul Peter Choi

aus Jeonju, Korea (R.O.K.)

Basel, 2004

Genehmigt von der Philosophisch-Naturwissenschaftlichen Fakultät auf Antrag der Herren Professoren:

Prof. Dr. C. Schönenberger
Prof. Dr. E. Sukhorukov

Basel, den 28. September 2004

Prof. Dr. Hans-Jakob Wirz, Dekan

To my Abba, Father in heaven

# *Contents*


**1 Introduction** **7**

**2 Transport properties of mesoscopic S-N junction** **11**

2.1 Current fluctuations . . . . . 11

2.1.1 Thermal noise . . . . . 11

2.1.2 Shot noise . . . . . 12

2.2 Shot noise in mesoscopic conductor . . . . . 14

2.3 Mesoscopic S-N junction . . . . . 17

2.3.1 General properties of S-N junctions . . . . . 17

2.3.2 Shot noise in S-N junction . . . . . 20

2.4 Cross-correlation in multi-terminal hybrid S-N beam splitter . . . . . 21

**3 Sample Preparation** **25**

3.1 Micro-fabrication process . . . . . 25

3.1.1 Electron-beam lithography . . . . . 26

3.1.2 Metallization and etching technique . . . . . 27

3.2 InAs-Heterostructures . . . . . 29

3.2.1 Ohmic contact . . . . . 30

3.2.2 MESA and fine etching . . . . . 32

3.2.3 niobium deposition . . . . . 32

3.2.4 Bonding and final . . . . . 34

3.3 Characterization of the sample . . . . . 34

3.3.1 InAs 2-dimensional electron gas (2DEG) . . . . . 34

**4 Measurement setup** **39**

4.1 Low temperature measurement . . . . . 39

4.2 Noise measurement . . . . . 40

4.2.1 Low frequency noise detection scheme . . . . . 41

4.2.2 Characterization of the noise-measurement setup . . . . . 42

4.3 Gating of the InAs heterostructures . . . . . 47

**5 Shot noise in superconductor-semiconductor heterostructure junction 51**
5.1 Introduction . . . . . 51
5.2 Experiment . . . . . 53
5.3 Results . . . . . 56
5.3.1 Resistance measurements . . . . . 56
5.3.2 Shot-noise measurements . . . . . 59
5.4 Discussion and Modelling . . . . . 62
5.5 Outlook and conclusions . . . . . 68

**A Calculation of the transfer function 69**

**B Process recipes 75**

## Chapter 1

# *Introduction*

Shot noise in a mesoscopic electrical conductor have become one of the most attention-drawing subject over the last decade. This is because the shot-noise measurements provide a powerful tool to study charge transport in mesoscopic systems [1]. While conventional resistance measurements yield information on the average probability for the transmission of electrons from source to drain, shot-noise provides additional information on the electron transfer process, which can not be obtained from resistance measurements. For example, one can determine the charge '$q$' of the current carrying quasi-particles in different systems from the Poisson shot noise $S_I = 2q\langle I\rangle$ [2] where $\langle I\rangle$ is the mean current of the system. For instance, the quasi-particle charge is a fraction of the electron charge '$e$' in the fractional quantum Hall regime [3, 4, 5]. The multiple charge quanta were observed in an atomic point contact between two superconducting electrodes [6].

Shot-noise also provides information on the statistics of the electron transfer. Shot noise in general is suppressed from its classical value $S_I = 2e\langle I\rangle$, due to the correlations. In mesoscopic conductors, due to the Pauli principle in fermion statistics, electrons are highly correlated. As a results, the noise is fully suppressed in the limit of a perfect open channel $T = 1$. For the opposite limit of low transmission $T \ll 1$, transmission of electron follows a Poisson process and recovers the Schottky result $S_I = 2e\langle I\rangle$ [2]. For many channel systems, shot-noise is suppressed to $1/2 \times 2e\langle I\rangle$ for a symmetric double barrier junction [7, 8], to 1/3 in a disordered wire [9, 10, 11, 12, 13, 14] and to 1/4 in an open chaotic cavity [15, 16, 17].

When a superconductor is involved, the shot-noise can be enhanced by virtue of the Andreev reflection process taking place at the interface between a normal metal and a superconductor. In some limiting cases, e.g. in the tunneling and disordered limit, the shot-noise can be doubled with respect to its normal state value [18, 19, 20, 21]. One of the main results of this thesis is an extensive comparison of our experimental data on conductance and shot noise measurements in a S-N junction with various theoretical models.

In addition to measure shot-noise in a two-terminal geometry, one can also perform the fluctuation measurements on multi-terminal conductors. Whereas shot-

noise corresponds to the autocorrelation of fluctuations from the same leads, cross-correlation measurements of fluctuations between different leads provide a wealth of new experiments. For example, the exchange-correlations can be measured directly from these geometry [22]. Experimental attempt in mesoscopic electronic device was the correlation measurements [14, 23] on electron beam-splitter geometry [24] which is the analogue to the Hanbury-Brown Twiss (HBT) experiment in optics. In their experiment, Hanbury-Brown and Twiss demonstrated the intensity-intensity correlations of the light of a star in order to determine its diameter [25]. They measured a positive correlations between two different output photon beams as predicted to the particles obeying Bose-Einstein statistics. This behavior is often called '*bunching*'. On the other hand, a stream of the particles obeying Fermi-Dirac statistics is expected to show a *anti-bunching* behavior, resulting in a negative correlation of the intensity fluctuations. Latter one was confirmed by a Fermionic version of HBT experiments in single-mode, high-mobility semiconductor 2DEG systems [14, 23].

Whereas in a single electron picture, correlations between Fermions are always negative[1] (anti-bunching), the correlation signal is expected to become positive if two electrons are injected simultaneously to two arms and leave the device through different leads for the coincident detection in both outputs[2]. One simple example is the splitting of the cooper pair in a Y-junction geometry in front of the superconductor. Fig.1.1 shows the possible experimental scheme of the correlation measurement as described here and the sample realized in an high-mobility semiconductor heterostructures. Since all three experiments were done[3], only one left unfolded, '*The positive correlations from the Fermionic system*'. The main motivation of this thesis work was to find a positive correlations in the device shown in Fig.1.1. In a well defined single channel collision experiment on an electron beam splitter, it has theoretically been shown that the measured correlations are sensitive to the spin entanglement [29, 30]. This is another even more exciting issue and we would like to mention that the experimental quest for positive correlations is important for the new field of quantum computation and communication in the solid state, [31, 32] in which entangled electrons play a crucial role. A natural source of entanglement is found in superconductors in which electrons are paired in a spin-singlet state. A source of entangled electrons may therefore be based on a superconducting injector.[33, 34, 27, 35, 36, 37, 38, 38, 39, 40, 41] Even more so, an electronic beam-splitter is capable of distinguishing entangled electrons from single electrons.[29, 42] However, the positive correlations have not been observed in solid-state mesoscopic devices until today.

[1]This statement, however, needs some assumptions to be completely correct. See Ref.[26] and references there in for the detailed discussions on this issue.

[2]It is also true for some multi-channel cases if tunneling is systematically controlled by intermediate quantum dots, e.t.c. See for example, Ref.[27]

[3]The photon anti-bunching, i.e. negative correlations with single photon source was also experimentally shown recently by Yuan et al.[28]

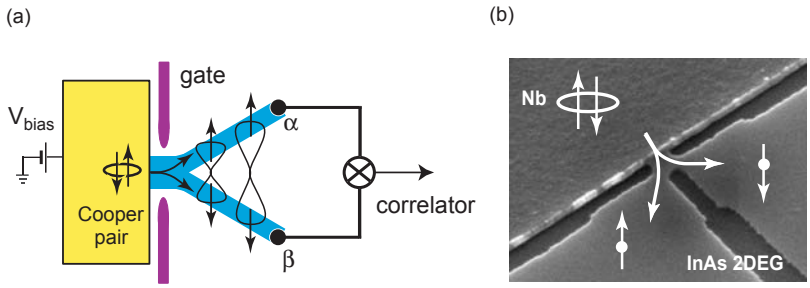


**Figure 1.1**: (a)Possible scheme of cross-correlation measurements between two different leads connected to a superconductor as an injector of correlated pairs to the normal side. (b) A sample realization in a High mobility 2-dimensional electron gas (2DEG) system having a mesoscopic beam splitter (Y-junction) with a superconducting (Nb) contact.

This thesis is organized as follows. Chapter 2 is devoted to the theoretical background of the electrical transport and the current fluctuations. We introduce the basic concept of electrical transport and the shot noise in normal state and superconductor-normal metal (S-N) junction. We also briefly review the theoretical proposals and arguments about the current-current cross-correlations in three-terminal systems. In Chapter 3, we describe the sample fabrication techniques which have been done in our laboratory such as e-beam lithography, metallization and etching. We present also the characterization of our particular system, niobium (Nb) / InAs-based 2DEG junction. Chapter 4 describes the reliable low-temperature measurement technique for detecting the noise. We characterize our measurement setup using a simple $RC$-circuit model. In Chapter 5, our main results about the shot noise of S-N junction are presented in detail.

# Chapter 2

# *Transport properties of mesoscopic S-N junction*

## 2.1 Current fluctuations

Electronic current noise are dynamical fluctuations $\Delta I(t) = I(t) - \langle I \rangle$ of the electrical current $I(t)$ around it's time averaged mean value $\langle I \rangle$. Here, the brackets $\langle ... \rangle$ indicate an ensemble average for ergodic system. Noise is characterized by its power spectral density $S(\omega)$, which is the Fourier transform at a certain frequency $\omega$ of the current-current correlation function,

$$S(\omega) = 2 \int_{-\infty}^{\infty} dt \; e^{i\omega t} \langle \Delta I(t + t_0) \Delta I(t_0) \rangle \tag{2.1}$$

Two essential noise sources[1] which appear in the fluctuations of the occupation numbers of states are thermal fluctuations from the thermal agitation of electric charges and shot noise (partition noise) due to the quantized nature of the charge carriers.

### 2.1.1 Thermal noise

At finite temperature ($T \neq 0$), the thermal agitation of electric charges is present in every conductor and becomes an unavoidable source of noise even in the absence of the bias current (i.e. in equilibrium). These thermal fluctuations are called thermal noise and also known as Johnson-Nyquist noise because they were first reported experimentally by J. B. Johnson [43] and analyzed theoretically by H. Nyquist [44]. Nyquist relation can be derived from a simple classical model of a short-circuit resistor. Consider a resistor $R$ shunted by a capacitor $C$ in Fig. 2.1. In equilibrium, an average energy of $C\langle U^2 \rangle / 2 = k_B T/2$ is stored in the capacitor. The voltage fluctuation U at the time $t_0$ decays with a characteristic $RC$-time and causes current

[1] We do not consider $1/f$ noise here.

fluctuations in the resistor

$$I(t) = \frac{U}{R} e^{-(t-t_0)/RC} \qquad \text{for} \qquad t > t_0 \tag{2.2}$$

Substituting this $I(t)$ behaviour into Eq. 2.1 yields,

$$S_I(\omega) = 4 \int_0^\infty dt\ e^{iwt} \frac{\langle U^2 \rangle}{R^2} e^{-t/RC}\,. \tag{2.3}$$

Since $\langle U^2 \rangle = k_B T/C$, we get

$$S_I(\omega) = \frac{4k_B T}{R} \cdot \frac{1}{1 - i\omega RC}\,. \tag{2.4}$$

In the low frequency limit, $\omega \ll (RC)^{-1}$, we obtain for the thermal noise of a resistor $R$,

$$S_I = \frac{4k_B T}{R}\,. \tag{2.5}$$

We see that thermal noise does not provide additional information on the system beyond that already known from conductance measurements. However, thermal noise is useful for calibrating the experiment setup to extract correct data.

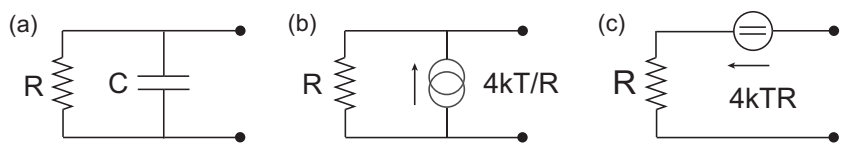


**Figure 2.1**: (a)$RC$-circuit for deriving the thermal noise of a resistor $R$ in thermodynamic equilibrium with the environment. (b) Equivalent circuit with a current noise source in parallel. (c) Equivalent circuit with a voltage noise source in series with a resistor $R$.

### 2.1.2 Shot noise

Shot noise in an electrical conductor is a non-equilibrium (Bias voltage $V \neq 0$) noise originated from the discreteness of the charges of electrical current. Shot noise was first described by Schottky [2] who studied the charge-fluctuation phenomena in a vacuum tube diode. In his work, he found a simple relation between the power spectral density of current fluctuations $S_I$ and the mean value of the current $\langle I \rangle$ known as Schottky formula $S = 2e\langle I \rangle$ where $e$ is the unit of the electron charge. The same relation is valid in mesoscopic tunnel junctions with a high barrier of the interface. In this case, we can derive the Schottkey's formula in a simple manner. Since there are only two possible outcomes from the tunnelling experiment i.e., transmission with probability ($\Gamma$) or reflection with probability $(1 - \Gamma)$, the shot noise in a single

barrier with transmission probability $\Gamma$ can be described as a simple bimodal distribution from the classical statistics. The probability to have $n_\Gamma$ transmitted particles at time interval $t$ is,

$$P_{binomial} = \begin{pmatrix} n \\ n_\Gamma \end{pmatrix} n_\Gamma \Gamma^{n_\Gamma} (1-\Gamma)^{n-n_\Gamma} \,. \tag{2.6}$$

where $n$ is the total number of charge quanta $q$ incident on the barrier. The average of the transmitted particles $\langle n_T \rangle$ equals $n\Gamma$ and the variance is given by

$$\begin{aligned} \langle \Delta n_\Gamma^2 \rangle &\equiv \langle n_\Gamma^2 \rangle - \langle n_\Gamma \rangle^2 = n\Gamma(1-\Gamma) \\ &= \langle n_\Gamma \rangle (1-\Gamma) \,. \end{aligned} \tag{2.7}$$

Since $I = n_T q/t$, where $q$ is the charge of each particle, the variance of the total current is $\langle \Delta I^2 \rangle = q\langle I \rangle (1-\Gamma)/t$ . Using Eq. 2.1, for $\omega \ll t^{-1}$, the frequency independent shot noise power is

$$S_I = 2q\langle I \rangle \cdot (1-\Gamma) \,. \tag{2.8}$$

In the limit of very low transmission ($\Gamma \ll 1$), i.e., $n_\Gamma \cdot \Gamma \ll n_\Gamma$ in Eq. 2.6, the binomial distribution can be approximated by the Poisson distribution. In this case, shot noise can be written by the well known Schottky formula [2] :

$$S_I = S_{Poisson} \equiv 2q\langle I \rangle \,. \tag{2.9}$$

More generally, the Poisson noise is valid for a '*dilute stream of uncorrelated particles*' each carrying a charge quantum $q$. The correlations among the charge carriers, for instance Pauli exclusion principle in Fermionic statistics or Coulomb interaction suppress the shot noise value below $S_{Poisson}$. To characterize the suppression of shot noise compared to the Poisson value, one defines the Fano factor $F$ :

$$F \equiv \frac{S_I}{2e\langle I \rangle} \,. \tag{2.10}$$

## 2.2 Shot noise in mesoscopic conductor

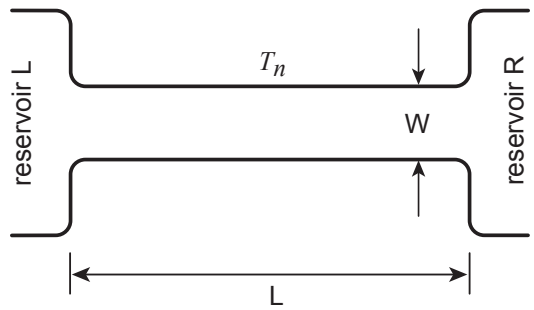


**Figure 2.2**: The two-terminal conductor

Let us consider coherent transport in a mesoscopic conductor connected to two reservoirs left(L) and right(R) (Fig.2.2). Reservoirs are considered to be in a thermal equilibrium and no phase memory of the carriers will be remain. The reservoirs act as sources of carriers determined by a Fermi distribution function but also can be a perfect sinks of carriers irrespective of the energy of the carrier that is leaving the conductor. For a macroscopic sample, the conductance is given by Ohmic scaling law : $G = \sigma W/L$ where $\sigma$ is the conductivity, $W$ is the width and $L$ is the length of the wire. When the dimension of the sample is getting smaller, so that $W$ becomes of the order of the Fermi wavelength $\lambda_F$, the conductance does not decrease linearly with the width. Instead it depends on the number of eigen-modes in the conductor and shows the quantized steps [45]. This can be described by so called 'Landauer formula' first derived by Landauer [46] for a 1-D conductor. The generalized multi-channel Landauer formula at zero-temperature for a small applied voltage is given by [47]

$$G = \frac{2e^2}{h} \sum_{n=1}^{N} T_n \,, \tag{2.11}$$

with $N$ the number of scattering channels at the Fermi energy and $T_n$ the eigenvalue of transmission coefficients. The zero-temperature shot noise power is then given by [22],

$$S = 2eVG_0 \sum_{n=1}^{N} T_n(1 - T_n) \,, \tag{2.12}$$

where $G_0$ is the conductance quantum which the maximum value for single channel can have and equals to $2e^2/h$. The shot noise is not simply determined by the conductance of the sample but contains the products of $T_n(1-T_n)$ i.e., transmission and reflection probabilities of the eigen-channels. From this equation it is obvious that the zero-temperature shot noise for a non-interacting system is always suppressed

compared to the Poisson value. Either completely opened eigen-channel (for which $T_n = 1$) or completely closed one ($T_n = 0$) does not contribute to the shot noise, whereas $T_n = 1/2$ yields the maximum value. In the limit of low transparency, $T_n \ll 1$ for all n, the shot noise is given by the Poisson form,

$$S_{Poisson} = 2eVG_0 \sum_{n=1}^{N} T_n = 2e\langle I \rangle \,. \tag{2.13}$$

In terms of the transmission probabilities, the Fano factor has the form,

$$F_N = \frac{S}{S_{Poisson}} = \frac{\sum_n T_n(1-T_n)}{\sum_n T_n} \,. \tag{2.14}$$

The Fano factor varies from zero (all channels are fully open) to one (Poissonian limit). For a single channel system, it becomes $1 - T$. The general results of the noise power for non-zero voltage and non-zero temperature is

$$S = 2G_0 \sum_{n=1}^{N} \left[ 2k_B \mathrm{T} T_n^2 + T_n(1-T_n) eV \coth\left(\frac{eV}{2k_B \mathrm{T}}\right) \right] , \tag{2.15}$$

where $V$ is the voltage applied over the two terminal conductor. Note that the general noise expression above is not a simple superposition of thermal and shot noise. For a tunnel barrier, all the transmission coefficients are small, $T_n \ll 1$. Substituting the Possionian shot noise in Eq.2.15, we obtain

$$S = 2eVG_0 \sum_{n=1}^{N} T_n \coth\left(\frac{eV}{2k_B \mathrm{T}}\right) = S_{Poisson} \coth\left(\frac{eV}{2k_B \mathrm{T}}\right) , \tag{2.16}$$

The crossover from thermal noise to full Poisson noise occurs at $eV \approx k_B T$ independent of any details of the conductor. This behavior has been observed in various systems. See for example Birk et al.[48] who measured noise in a tunnel barrier between a STM tip and a metallic surface.

### Two examples

The results described above are valid for conductors with arbitrary (elastic) scattering transmission eigenvalues $T_n$. Once the transmission eigenvalues are known (e.g. the distribution function $\rho(T)$ of the transmission eigenvalues), we can calculate the average conductance $\langle G \rangle$ and the shot noise $\langle S \rangle$ of the system with the following integration (The generalization of Eq. 2.11 and Eq. 2.12) :

$$\langle G \rangle = G_0 N \int_0^1 dT \rho(T) T \tag{2.17}$$

$$\langle S \rangle = 2eVG_0 N \int_0^1 dT \rho(T) T(1-T) \,. \tag{2.18}$$

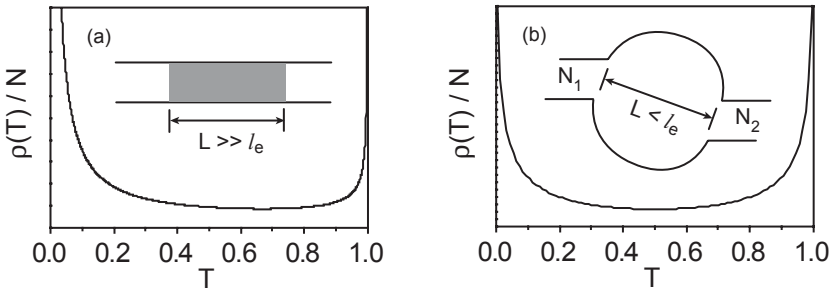


**Figure 2.3**: The distribution function of transmission eigenvalues $T$ and the schematics for two example cases. (a) a diffusive conductor according to Eq.2.19 with $L = 15\ l_e$. (b) a chaotic cavity according to Eq.2.20 with $N_1 = N_2 = N$.

Now let us consider two systems. The first one is a *Metallic diffusive wire* with length $L$ much greater than the mean free path $l_e$. In a diffusive conductor, electrons are scattered elastically by randomly distributed impurities or the grain boundaries. Thus, the energy is conserved but the momentum vector and the phase are changed. The second system is a *Chaotic cavity* with the size smaller than the mean free path $l_e$ so that electrons scatter ballistically within the cavity. The cavity is connected via two ballistic (noiseless) point contacts to the reservoirs on both sides (The systems are shown schematically in the insets of the Fig.2.3). The distribution functions for the transmission eigenvalues $T_n$ of both systems are given by (from the review in Ref.[49])

$$\rho(T)_{\text{diffusive}} = \frac{l_e}{2L}\frac{1}{T\sqrt{1-T}} \quad : \quad \text{Diffusive wire} \tag{2.19}$$

$$\rho(T)_{\text{cavity}} = \frac{1}{\pi}\frac{1}{\sqrt{T(1-T)}} \quad : \quad \text{Chaotic cavity}\,. \tag{2.20}$$

The two distributions are plotted in Fig.2.3. For the chaotic cavity, we only consider symmetric case here i.e. two point contacts in left and right sides are identical ($N_1 = N_2 = N \gg 1$. See Fig.2.3b). They are both bimodal distributions with one peak at $T \lesssim 1$ and the other at $T \gtrsim 0$ i.e., large number of almost open channels and almost closed channels. Using Eq. 2.17 and Eq. 2.18 with the distribution functions given above, one can obtain the average conductance and the shot noise power for the diffusive wire,

$$\langle G\rangle = G_0\frac{Nl_e}{L} \quad , \quad \langle S\rangle = 2eVG_0\frac{Nl_e}{3L} = \frac{1}{3}S_{Poisson} \tag{2.21}$$

and for the open chaotic cavity,

$$\langle G\rangle = G_0\frac{N}{2} \quad , \quad \langle S\rangle = \frac{1}{4}S_{Poisson}\,. \tag{2.22}$$

The average conductance for diffusive wire is just Drude formula with $N$ number of eigen-channels. The suppression of the shot noise result by a factor one-third (diffusive wire) and one-quarter (Chaotic cavity) are universal in a sense that they are independent on specific microscopic properties of the device.

## 2.3 Mesoscopic S-N junction

### 2.3.1 General properties of S-N junctions

#### Andreev reflection

When a normal conductor is connected to a superconductor, a conversion of the dissipative electrical current in the normal metal into a dissipationless supercurrent occurred at the interface. This phenomenon was first discovered by A.E. Andreev [50] and is known as '*Andreev Reflection*'. The mechanism of '*Andreev Reflection*' is depicted in Fig.2.4. An incident electron slightly above the Fermi level in the normal lead is reflected at the interface as a hole slightly below the Fermi level. The missing charge of $2e$ is added to a superconductor as a Cooper-pair at the Fermi level. The reflected hole has the same momentum as the incident electron and the velocity of the hole is the opposite of the velocity of the electron. Therefore, this process is called '*retro-reflection*'. Andreev reflection(AR) is a two-particle process, therefore the probability of Andreev reflection is described in terms of $T^2$ [49, 51]:

$$R_A = \frac{T^2}{(2-T)^2}\,, \tag{2.23}$$

and the corresponding conductance of an S-N junction is then,

$$G_A = \frac{4e^2}{h} \cdot R_A\,. \tag{2.24}$$

In ballistic junction ($T = 1$), $G_A = 4e^2/h = 2G_N$ is the double of the normal conductance $G_N$ and in the tunnelling limit ($T \ll 1$), $G_A = e^2/h\ T^2 \ll G_N$. We will discuss this behavior further in the next section.

#### The spectral conductance

When a potential barrier is introduced at the S-N interface, Andreev reflection probability, $R_A$ is found to be less than one because now the normal reflection (specular reflection of the electron) also can happen. This problem was first studied by Blonder, Tinkham and Klapwijk in a 1-D ballistic S-N junction and their results are known as BTK model [52]. In the BTK model, the potential barrier at the S-N interface is approximated by a $\delta$-shape barrier, the interface is characterized by a single transparency and a step-like increase of the superconducting pair potential

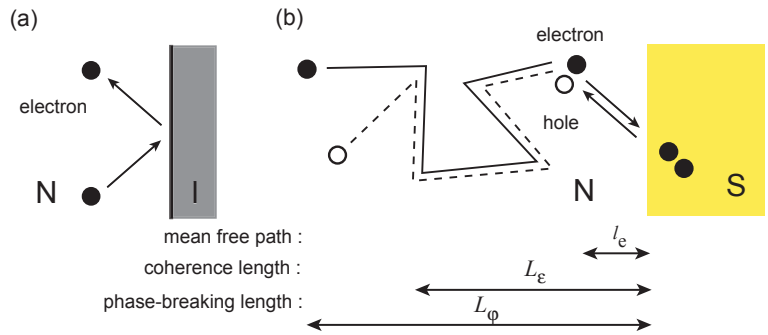


**Figure 2.4**: (a)Normal reflection by an insulator (b)Andreeve reflection by a superconductor. The retro-reflected hole takes the same path as the incident electron in reverse. Some relevant length scales are depicted.

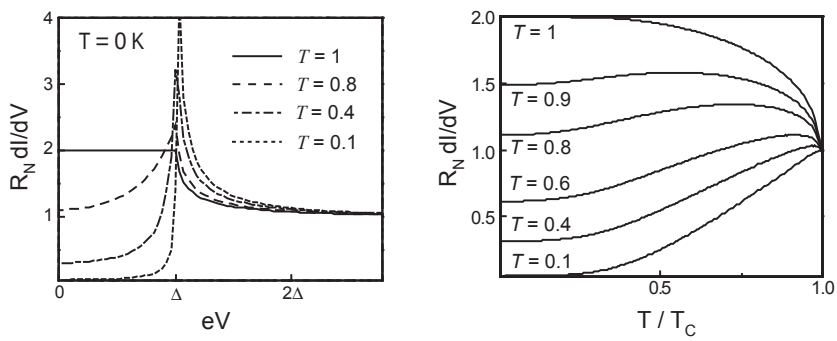


**Figure 2.5**: (a) Voltage dependent differential conductance in units of normal-state conductance for various transmission coefficient $T$. It shows the continues variation from metallic to tunnelling limit.(b) Zero-bias differential conductance normalized by normal-state conductance versus temperature for different transmission coefficients $T$.

is assumed at the interface. More recently, Cuevas et.al [53] found an equivalent expression to the BTK model through a single-mode contact between a superconductor and a normal metal using so called 'Hamiltonian approach' combination with the non-equilibrium Green function technique. They considered the case $L_\varphi \gg L$ where $L_\varphi$ is phase breaking length and $L$ is the sample length (see Fig. 2.4) so that the spectral current is constant along the sample [54]. In this regime, we can write the spectral current as a function of the spectral conductance $G_{NS}(E)$ and the difference of distribution function $f$ between the right and left reservoirs :

$$I(V, \mathrm{T}) = \frac{1}{e} \int dE \; G_{NS}(E)(f(E - eV) - f(E)) \,. \tag{2.25}$$

The current expressed through the spectral conductance $G_{NS}(E)$ is a function of applied voltage $V$ and temperature T. The bias dependent spectral conductance for

the single channel case (at T = 0) is given by [53]

$$G_{NS}(V,0) = \frac{4e^2}{h} \begin{cases} \frac{T^2}{(2-T)^2-4(1-T)(eV/\Delta)^2} & eV \leq \Delta\,, \\ \frac{T^2}{T+(2-T)\sqrt{1-(\Delta/eV)^2}} & eV > \Delta\,. \end{cases} \tag{2.26}$$

Note that the spectral conductance $G_{NS}(V)$ varies between $(4e^2/h)T^2/(2-T)^2$ (Eq. 2.24) for $V = 0$ and $4e^2/h$ for $eV = \Delta$. At finite temperature, the differential conductance is the integral of the spectral conductance multiplied by the energy derivative of the Fermi distribution function [54]:

$$G_{NS}(V,\mathrm{T}) = \frac{1}{e}\int \frac{d\Delta f}{dV} G_{NS}(E)dE = \frac{1}{4k_B\mathrm{T}}\int dE \frac{G_{NS}(E)}{\cosh^2\left(\frac{E}{2k_B\mathrm{T}}\right)}\,. \tag{2.27}$$

We calculated both equations (Eq. 2.26 and Eq. 2.27 for T = 0) numerically to plot the bias dependent differential conductance $dI/dV(V)$ and temperature dependent linear conductance $dI/dV(\mathrm{T})$ curves. The results are shown in Fig.2.5 for a number of different transmission coefficient $T$.

### Proximity effect

The proximity effect between a normal metal and a superconductor is a consequence of the correlations induced in the normal metal by Andreev reflection. In order to study the diffusion of the Andreev pair (electron-hole pair) in the normal side, we consider a normal metal in dirty limit when the elastic mean free path $l_e$ is much smaller than the sample length $L$ and $L$ itself is smaller than the phase breaking length $L_\varphi$ ($l_e \ll L \ll L_\varphi$). Let us consider the trajectories of an electron incident to the N-S interface with the energy $\epsilon = E - E_F$ above the Fermi level and the reflected hole retracing the trajectory of the electron. The wave-vector mismatch $\delta k = \epsilon/\hbar v_F$ between the electron and the hole accumulate the phase difference between them. After the diffusion over a distance $L$ from the interface, the phase shift $2\delta kL$ between two particles is of order $\pi$ at a distance equal to the energy dependent coherence length given by $L_\epsilon = \sqrt{\hbar D/\epsilon}$. Here $\hbar$ is the Planck constant and $D$ is the diffusion constant in normal conductor. At the same time, the trajectories of electron and hole are shifted by a distance of order of the Fermi wavelength. Further diffusion of the two particles will be different and the pair will break apart. Therefore, this coherence length $L_\epsilon$ characterizes how far the two electrons from a Cooper pair leaking from the superconductor will diffuse in coherent maner in the normal metal. Electron-hole coherence is hence maintained in an energy range of $\epsilon_c = \hbar D/L^2$. This characteristic energy is called Thouless energy or correlation energy and is of great importance in proximity structures [55]. The proximity induced superconductivity is also dependent on the interface quality between superconductor and normal metal since the effect decays exponentially with the interface resistance.

### 2.3.2 Shot noise in S-N junction

Now, we turn to the shot noise in S-N junction. The conductance and the shot noise of an S-N junction are given by [49, 56]

$$G_{NS} = G_0 \sum_{n=1}^{N} \frac{2T_n^2}{(2-T_n)^2}\,, \tag{2.28}$$

$$S_{NS} = 2eVG_0 \sum_{n=1}^{N} \frac{16T_n^2(1-T_n)}{(2-T_n)^4}\,, \tag{2.29}$$

As for the normal case, scattering channels with $T_n = 0$ and $T_n = 1$ does not contribute to the shot noise. However, the intermediate transmission channels contribute quite differently than in the normal case (Eq. 2.12). We obtain for the Fano factors for S-N junction,

$$F_S = \frac{S_{NS}}{2eVG_{NS}} = \sum_n \frac{16T_n^2(1-T_n)}{(2-T_n)^4} \Big/ \sum_n \frac{2T_n^2}{(2-T_n)^2}\,. \tag{2.30}$$

In the case when all the eigen-channels are non-interacting and $T_n = \Gamma$ for all $n$, shot noise can be written as [57]

$$S_{NS} = 2eVG_0N\frac{16\Gamma^2(1-\Gamma)}{(2-\Gamma)^4} = \frac{8(1-\Gamma)}{(2-\Gamma)^2}S_{Poisson}\,. \tag{2.31}$$

For low-transparency $\Gamma \ll 1$, this simplifies to the double of the Poisson noise $S_{NS} = 2S_{Poisson}$. Similar to the normal case, this can be interpreted as the result of uncorrelated transfer of charge $2e$. Since Eqs.2.28 and Eq.2.29 are valid for arbitrary scattering region [49], we can integrate Eqs.2.28 and Eq.2.29 over the distribution function of the transmission coefficients given by Eq.2.19 and Eq.2.20 as we did in the normal-state :

$$G_{NS} = G_0N\int_0^1 dT\rho(T)\frac{2T^2}{(2-T)^2} \tag{2.32}$$

$$S_{NS} = S_0N\int_0^1 dT\rho(T)\frac{16T^2(1-T)}{(2-T)^4}\,. \tag{2.33}$$

For a disordered S-N junction, we find an average conductance which is equal to that of the normal state of the junction : $\langle G_{NS}\rangle_L = 2\langle G_N\rangle_{2L} = \langle G_N\rangle_L$ for $l_e \ll L \ll Nl_e$ [56] and the noise power having two times larger Fano factor than that of a normal diffusive wire:

$$S_{NS} = \frac{2}{3}S_{Poisson}\,. \tag{2.34}$$

For a (symmetric)chaotic cavity in series with a superconductor, we get [49, 51],

$$G_{NS} = G_0(2-\sqrt{2})N \tag{2.35}$$

$$S_{NS} = \frac{1}{4(\sqrt{2}-1)} S_{Poisson} \approx 0.6\ S_{Poisson}\,. \tag{2.36}$$

De Jong and Beenakker [51] studied in the case of a disordered N-S junction with a tunnel barrier at the interface. They described the crossover between the two limits which are Ballistic (Eq.2.29) and a diffusive (Eq.2.34) limit for the normal metal. They found out that only for two particular cases namely, for a high tunnel barrier and for a diffusive N-S junction, the Fano factor is doubled with respect to the normal state value. For other cases, the ratio $F_S/F_N$ is more complicated. We come to this point later in Chapter 5 and discuss it in more detail in order to interpret our shot noise results in S-semiconductor 2DEG structure.

## 2.4 Cross-correlation in multi-terminal hybrid S-N beam splitter

So far, we have considered only current fluctuation measurements in a two-terminal geometry. However, one can measure the noise in the multi-terminal cases, i.e., cross-correlations of fluctuations between different leads [22] and this provides a wealth of new experiments. In this section, we will restrict ourselves to the case of three-terminal device and when the shot noise is expressed in terms of transmission probabilities only. As the shot-noise measurement provides the information on the statistics of the electron transfer, the cross-correlation measurements are also expected to yield the different results for the systems obeying different statistics. The well known example is the famous optical experiment by Hanbury-Brown and Twiss (HBT) [25]. In the HBT experiment, Hanbury-Brown and Twiss measured the intensity-intensity correlations of the light of a star in order to determine its diameter [25]. In a subsequent laboratory experiment, the light of a mercury vapor lamp was divided by a half-silvered mirror into a transmitted and a reflected beam whose intensity were measured by the two detectors [58]. They measured positive correlations as long as the two beams are phase-coherent. This positive correlations, found in their experiment, can be interpreted as an enhanced detection probability of two photons in coincidence. This behavior is often called *bunching* for the particles obeying Bose-Einstein statistics. On the other hand, the partitioning of a stream of particles obeying Fermi-Dirac statistics leads to an *anti-bunching* behavior due to the exclusion principle, resulting negative correlations of the intensity fluctuations. This was confirmed by a Fermionic version of HBT experiments in a single-mode, high-mobility semiconductor 2DEG systems [14, 23]. Furthermore, the bunching-like behavior (positive correlations) has been predicted theoretically in electronic multi-terminal devices in which at least one electrode is a superconductor [59, 60, 61, 27, 40, 62]. In the followings, We present briefly the relevant

theoretical proposals and arguments for the detection of positive correlations in the three terminal S-N beam splitter geometry.

Martin showed theoretically that when the junction contains no disorder, so there is only pure Andreev reflection happens, the noise correlation vanish [60]. This argument leads to the fact that the presence of disorder in S-N interface enhances the positive correlations in Fermionic system with a superconducting injector [60, 61]. In Ref. [61], the authors used BTK model to characterize the S-N interface with increasing barrier height and found large enhancement of noise correlations. Burkard et. al. showed Spin-singlet state leading to a bunching behavior enhances the noise correlations [29]. In the successive paper by Recher et.al. [27], a setup that involves a superconductor coupled to two quantum dots are proposed. See Fig. 2.6.(b). In their setup, the Cooper pair is breaking up and each electron penetrates separately through different normal leads. A simultaneous emission of the two electrons at different normal out-puts will make a positive correlations.

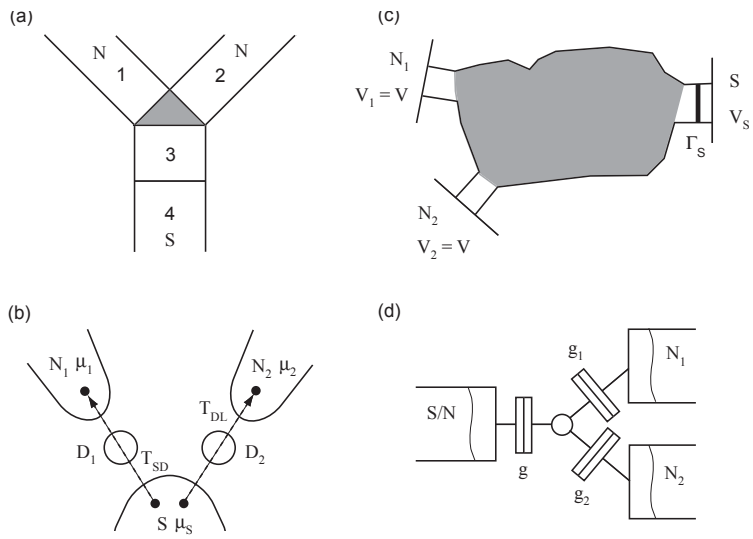


**Figure 2.6**: Schematics of different theoretical models for detecting positive correlations. (a) The sample schematics from Ref.[60] and [61]. Andreev reflection is between 3 and 4. The shaded triangle present a beam splitter. (b) The two spin-entangled electrons forming a Cooper pair tunnels from the superconductor, S, to two dots $D_1$ and $D_2$ (From Ref. [27]). The Dots are coupled to normal leads $N_1$ and $N_2$ with tunnelling amplitude $T_{DL}$. $\mu_i$ denotes the chemical potentials in three leads. (c) A chaotic quantum dot connected to one superconductor and two normal leads via quantum point contacts (Ref.[40]). $\Gamma_s$ is for the presence of normal backscattering at the S-N interface. (d) Three terminal beam splitter from Ref. [62]. All three terminals are connected by tunnel junctions with conductance $g, g_1$ and $g_2$ via a small normal island.

More recently, the same authors showed that if the normal leads are resistive, the probability for two electrons to tunnel into the same lead is suppressed because the dynamical Coulomb blockade effect is generated between the leads [63]. Ref. [62] considered a system which three terminals are connected by tunnel junction to a cental channel-mixing island (tunnel limit). They found large positive cross-correlations of the currents in the two normal terminals in a wide parameter range taking the proximity effect into account. A system consisting of a chaotic quantum dot connected via quantum point contact to one superconducting and two normal leads is considered in Ref. [40]. The authors found the large positive correlations for wide range of junction parameters and this was survived even in the absence of a proximity effect for non-ideal S-N interface. From their calculations, the correlation was enhanced by normal backscattering at the S-N interface. However, if the interaction plays a crucial role in the system, the simple connection between statistics and the sign of current-current correlations is not valid anymore [26].

In summary, we presented the number of theoretical proposals/arguments that support for measuring the positive correlations. It is preferable for the nature [2]to show us the *positive* sign in our correlation experiment in particular, the three terminal S-N beam splitter geometry.

[2]Of course, this holds clearer in the simplest case and this is why we need very reliable measurement technique avoiding any unwanted noise sources. At the same time, the measurement setup should be sensitive enough to detect very small fluctuations which we want to measure eventually.

## Chapter 3

# *Sample Preparation*

### 3.1 Micro-fabrication process

In order to investigate the quantum phenomena, the sample should be small enough so that the interesting quantum effect is dominant over the classical effects[1]. For this, a sub-micrometer patterning is required and recent development of the fabrication technology make this possible to realize a sub-micrometer size features on an electronic circuit chip. In this chapter, we will describe the micro/sub-micro fabrication techniques to make our mesoscopic S-N hybrid device as follows:

- InAs based semiconductor hetrostructure was fabricated using a molecule beam epitaxy (MBE) technique.
- A low-resistive ohmic contact to the 2DEG was made by depositing and alloying the Au-Ge-Ni multilayer on the 2DEG wafer.
- MESA area was formed by Electron-beam lithography combined with etching technique.
- A clean junction between 2DEG and superconductor was made by shadow angle evaporation of niobium(Nb). The angle evaporation ensures an side-contact between Nb and 2DEG layer (See the sample layout in Fig.3.5).
- Finally, a sub-micron Y-branch beam splitter was made by electron-beam lithography combined with a wet etch.

Fig. 3.1. shows an example of original sample layout and the final sample structure after the fabrication process. For next two sub-sections, we will briefly introduce the lithography technique, metallization and etching technique before we continue with our sample processing.

[1]Most of cases, we also need a low temperature in order to see the quantum effect in such a small structure and we will discuss about the low temperature measurement in next chapter

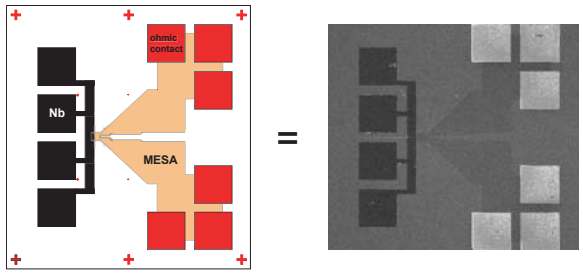


**Figure 3.1**: An example of sample layout(Left) and real structure after the main fabrication process(Right).

### 3.1.1 Electron-beam lithography

Lithography is the key technique to transfer the designed pattern onto the surface of a solid materials such as a silicon or other semi-conductor substrate. There are many different lithography techniques depend on which kind of source is used to produce a beam of using. The most widely known lithography technique amongst is UV(Photo)-lithography and Electron-beam lithography(EBL). In industry, Photo-lithography is widely used because it allows a mass production of the Integrated Circuit(IC) chips but It needs a Pre-patterned Mask and the resolution is limited by the wavelength of UV ray. EBL is an high-resolution patterning technique with high-energy electron beams expose onto the electron-beam sensitive resists [2]. Since the quantum mechanical wave lengths of high-energy electrons are very small, the resolution of the e-beam lithography is not limited by the diffraction of the beam.

Fig. 3.2 shows a block diagram of a typical electron beam lithography system. At the top of the column, electrons are emitted from the filament and focused onto the substrate on the specimen stage. The column is responsible for forming and controlling the electron beam with many elements such as electro-magnetic lenses for deflecting the beam, a blanker for turning the beam on and off, a stigmator for correcting any astigmatism in the beam, apertures for helping to define the beam, alignment systems for centering the beam in the column, and an electron detector for inspecting the structures on the sample. Underneath the column, there is a chamber containing a specimen stage for moving, rotating and tilting the sample inside and also the loading and unloading facility is equipped. A vacuum system, associated with the chamber is needed to maintain an appropriate vacuum level throughout the machine and during the load and unload cycles. A set of control electronics supplies power and signals to the various parts of the machine and the water cooling lines keeps the temperature for the electronics and the pumping system to work properly over the whole stage. Finally, the system is controlled by a computer with a lithography software, in our case, ELPHY *Quantum* from Raith GmbH. This

[2] PMMA (polymethyl methacrylate) is commonly used

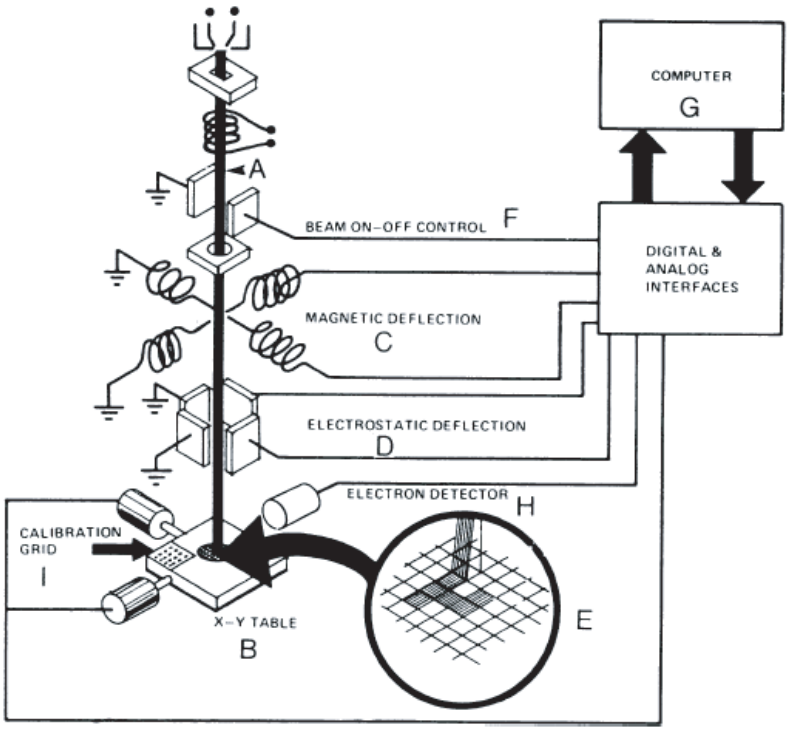


**Figure 3.2**: Schematic of typical e-beam lithography system. Descriptions are in the text.

lithography software controls the setting up the exposure job, loading and unloading the sample, aligning the electron beam, and sending pattern data to the pattern generator. In our lab, we have a Jeol JSM-IC848 SEM e-beam writer equipped with 2+ Motor control by Raith GmbH for a systematic movement of the specimen stage and house-made external field compensator.

In this thesis, Electron-beam lithography was used for making an Ohmic contact followed by evaporation(metallization), MESA definition and sub-micron beam splitter followed by wet etch. Typical lithography steps for both additive (i.e. metallization) and subtractive (i.e. etch) process are shown in Fig.3.3.

### 3.1.2 Metallization and etching technique

After the development of the resist, desired pattern can be formed by either subtractive (i.e. etch) or additive (i.e. metallization) way. In these ways, one can transfer their own structures to the substrate and finally make an electronic circuit. Metallization is the way to transfer the lithographically defined patterns onto the electronic circuit by depositing a thin metallic film on the substrate (Additive pattern transfer process). In industry, this is the most common way to make the metallic interconnections among the circuit elements together with the etching tech-

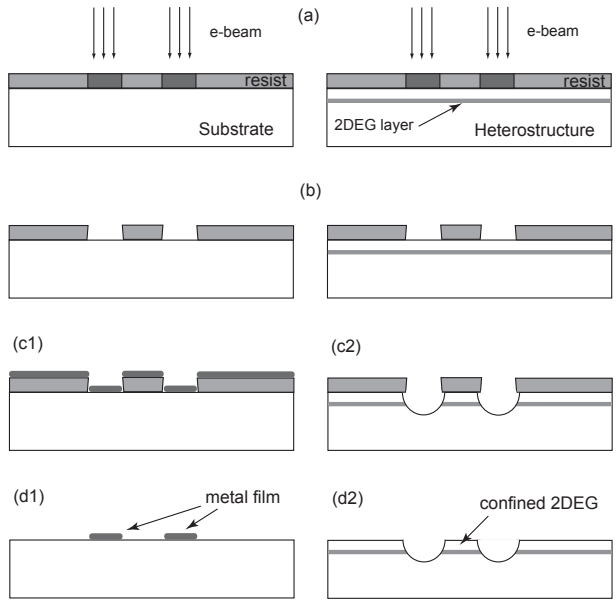


**Figure 3.3**: Typical lithography steps for additive (Left) and subtractive (Right) process. (a) Exposure of PMMA resist to e-beam (b) Development of PMMA. (c1) Evaporation of thin metals (c2) Etching of the heterostructure (d1) Lift-off (d2) Stripping

nique. There are a variety of metal deposition techniques in thin film technology but in our lab, we mostly use "Thermal evaporation".

A typical evaporation system has a vacuum chamber (Pressure is $\sim 10^{-5}$ Torr or better which is called HV ) contains a vapor source and a substrate. When the vapor source is heated, the vapor pressure of the evaporant (The metal to be evaporated, it is also often called 'target') becomes substantial and liberated atoms are sent out into the vacuum chamber and stick to the substrate where the metal film is formed. Among the different thermal evaporation systems, we use a *Balzers PLS* 500 system which uses electron-beam source to target the desired materials to be evaporated. The electron beam emitted from a heated wire (thermionic filament) is then focused by magnetic field and hits the surface of the evaporant which will be heated and evaporated. The vacuum of the evaporation chamber is typically $\lesssim 10^{-6}$mbar and using the Meissner cooling with liquid $N_2$, it can go down to $\lesssim 10^{-8}$mbar.

Etching is subtractive pattern transfer process from lithographically defined pattern. There are two available etching techniques in our lab, one is a wet etch using chemical solution (etchant) to dissolve the materials on the wafer surface and the other one is a Reactive Ion Etch (RIE)[3], which uses gaseous chemical etchant

[3]The name reactive ion etch is misleading since the gases in this etching process are not necessarily reactive. For instance, argon ions are frequently used to increase the ion bombardment and Argon is an inert gas which is not chemically reactive.

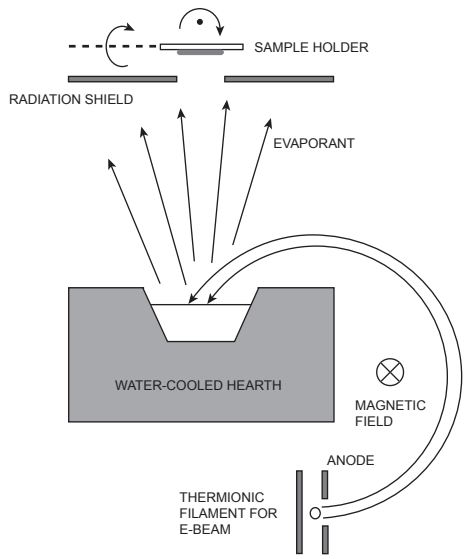


**Figure 3.4**: The schematics of *Balzers PLS* 500 thermal evaporation system.

like plasmas or ions. The wet etch usually has an isotropic etch profile while the dry(plasma) etch can give both isotropic and anisotropic etch profile depending on whether the etch process is purely chemical or physical. Plasma etch can be used for pre-cleaning of the substrate or removing the residual organic materials on the surface of the sample before evaporation. Actually, during our sample process, there is a oxygen plasma cleaning step just before the Au-Ge-Ni multilayer deposition (See section 3.2.1 for the details).

## 3.2 InAs-Heterostructures

Semiconductor two-dimensional electron gas (2DEG) system became very widely-used model system on short length scale such as mesoscopic or nanoscale conductors. This semiconductor 2DEG has a number of properties suitable for studying quantum effect in mesoscopic systems. It has an extremely low scattering rate and high electron mobility compare to those in bulk semiconductors or metal films. Its carrier density is also very low which means a large Fermi wavelength and the elastic mean free path can be found in 2DEG. In case of a GaAs-AlGaAs heterostructure 2DEG, the carrier density is $n_e = 4{\times}10^{11}\mathrm{cm}^{-2}$ and the mobility $\mu$ ranges from $\sim 10^4\mathrm{cm}^2/\mathrm{V{\cdot}s}$ to $\sim 10^6\mathrm{cm}^2/\mathrm{V{\cdot}s}$ . This can give the Fermi wavelength of $\lambda_F = 40$ nm and the mean free path $l_e$ from 10 nm up to 10 $\mu$m [64]! In our experiment, an InAs-inserted InAlAs/InGaAs heterostructures was used having InAs quantum well as a conducting 2DEG layer (Fig.3.5). InAs-based 2DEG has an higher carrier density and lower mobility than the GaAs based 2DEG $n_e = 2.1 \times 10^{12}\,\mathrm{cm}^{-2}$ and $\mu =$

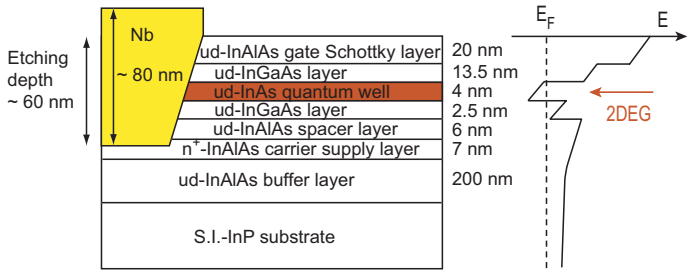


**Figure 3.5**: Schematic layer structure of an InAs-inserted InGaAs/InAlAs heterostructure with niobium contact and the corresponding energy band diagram.

$5 \sim 6 \times 10^4$ cm$^2$/V·s corresponding to a Fermi wavelength of $\lambda_F = 18\,\text{nm}$ and an elastic mean free path of $l_e = 1.2\,\mu\text{m}$. However, the advantage to use InAs 2DEG for our study in S-N hybrid structure was that the InAs 2DEG has no Schottky barrier when it forms a junction with a metal ensuring the good proximity effect in the normal side of the junction. InAs based heterostructures was fabricated by MBE technique at Basic research laboratory in NTT, Japan. MBE process is based on thermal evaporation of pure materials in an ultra high vacuum chamber (base pressure $\approx 10^{-11}$ mbar) and produces an high quality materials with extremely high carrier mobility. This heterostructure and its energy diagram is depicted in Fig.3.5 together with Nb-side contact.

### 3.2.1 Ohmic contact

Unlike the thin metal film, semiconductor heterostructure need a special way to have a 'good' ohmic contact. To make a good ohmic contact ensuring very low resistance and a linear current-voltage characteristics has been one of the very important requirements in developing the semiconductor heterostructure 2DEG device. Since a Schottky barrier is formed at the semiconductor-metal interface, a heat treatment is needed to alloy the metal into the surface of the semiconductor heterostructures in order to make a good ohmic contact. The Au-Ge-Ni multilayer is commonly used to make an ohmic contact to *n-type* GaAs systems [65] and we adapt this technique to our InAs-based heterostructure. Either by UV-lithography or e-beam lithography, we transfer the pattern into the substrate. After the exposing of the resist to the UV-light/e-beam, we develop the resist and get the desired pattern on the substrate[4]. Since the residual organic resist on the semiconductor surface will block the diffusion of metal alloy, before metal deposition, the patterned wafer is cleaned in the RIE chamber by oxygen plasma. During the oxygen plasma process, the oxide layer is formed on the semiconductor surface and this surface oxide also affect the

[4]See Fig.3.1 for the Ohmic contacts pattern(both layout and the real structure after the processing).

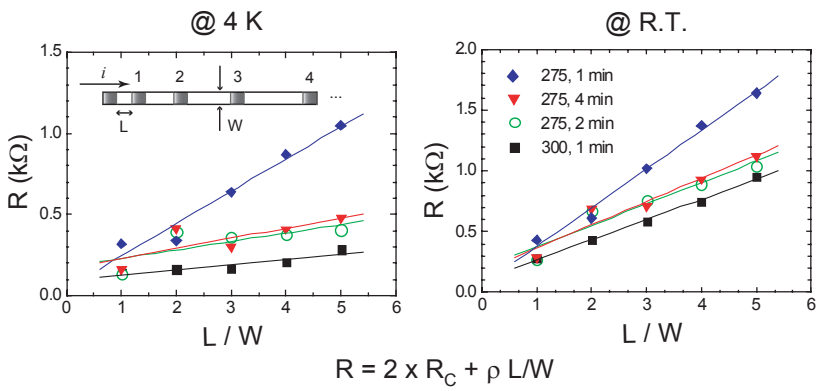


**Figure 3.6**: The plots of contact resistance $R_C$ and resistivity $\rho$ for different annealing temperatures and time. We can deduce the values $R_C$ and $\rho$ from y-intercept and slop of the linear plots. Left one is measured at liquid helium and right one is at room temperature. Inset of the left plot is the sample geometry for this check.

alloying reaction between Au-Ge-Ni and the heterostructure so, we remove oxide layer by dipping the sample in concentrate HCl solution (38 %). The metal layer structure of Ni/Au/Ge-Au/Ni with eutectic Au-Ge mixture of 88:12 wt% were evaporated in *Balzers PLS* 500 system. The deposition of first 6-nm-thick Ni layer of Au-Ge-Ni multilayer helps to have a low contact resist [66]. After the evaporation, the sample was alloyed in an annealing oven under the continuous flow of forming gas (90 % $N_2$ + 10 % $H_2$). Typical alloying temperature is 400 $\sim$ 500 °C for GaAs-based heterostructure. However, for InAs-based heterostructure, we have to use lower temperature because the heterostructure was formed at lower temperatures. The quality of the InAs 2DEG was degraded after the annealing of over 400 °C[5]. After the annealing of the multi-layer, we check the ohmic contact resistance and the resistivity (or sheet resistance) of the 2DEG both at room temperature(R.T.) and liquid helium temperature(4.2 K). We measure the resistance of the bar geometry consisted with a series of the square of length L and width W (Inset of Fig.3.6). We show the measured total resistance $R = 2R_C + \rho L/W$ versus $L/W$ in Fig 3.6. where $R_C$ is the contact resistance and $\rho$ is the resistivity of the 2DEG. From the linear fit of the data, we deduce contact resistance $R_C$ and the resistivity $\rho$. Table 4.1 summarize the data for few different annealing parameters to get the optimum value of $R_C$ and $\rho$.

[5]we measured contact resistance and resistivity for different annealing temperatures and found an optimum parameters.

**Table 3.1**: Summary of Ohmic-contact resistance and resistivity of the 2DEG for different annealing parameters (temperatures and time). It was checked at R.T. and 4.2 K respectively.

| Annealing condition | $R_C(\Omega)$ | | $\rho(\Omega)$ | |
|---|---|---|---|---|
| | R.T. | 4 K | R.T. | 4 K |
| 275°C, 1 min | 30 | 23 | 318 | 199 |
| 275°C, 2 min | 99 | 89 | 176 | 52 |
| 275°C, 4 min | 87 | 83 | 191 | 62 |
| 300°C, 1 min | 51 | 48 | 166 | 32 |

### 3.2.2 MESA and fine etching

Both large scale MESA definition and fine etching of the beam splitter geometry was formed by chemical wet-etch. We used $H_3PO_4 : H_2O_2 : H_2O = 1 : 1 : 100$ and this phosphoric etchant removes InAs based heterostructures isotropically and non-selectively. The etching rate for InAs-based heterostructure is $\sim 1$ nm/sec. As an alternative, $H_2SO_4 : H_2O_2 : H_2O = 3 : 1 : 100$ was used as well and it gives approximately the same etching rate. For the side-gating purpose, selective etching often used and one example is Citric acid : $H_2O_2$ = 1:1 [67]. This is selective for In(Ga)As against other layer materials. Fig.3.7 shows an example of large scale MESA area and fine etched lines with wet etchant.

### 3.2.3 niobium deposition

We choose the niobium as the superconducting side of our sample because it has a large superconducting gap and good stability under the thermal cycling. Semiconductor contact with niobium in particular with InAs-based heterostructure have

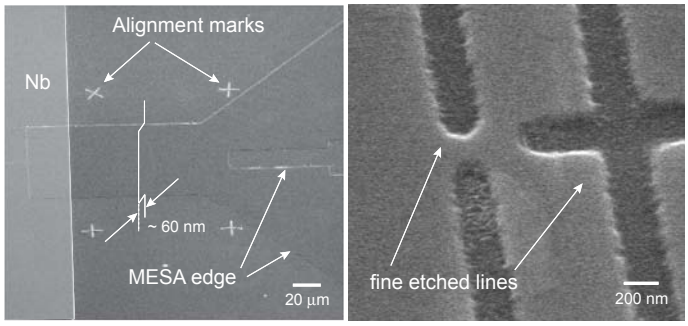


**Figure 3.7**: Left: MESA definition etch in prior to the beam splitter fine etch. Etching depth is about 60 nm. Right: Some examples of fine etched lines. Both are done by wet etching technique with isotropic and non-selective wet-etchant.

been fabricated intensively for studying the novel quantum effects in super-semi conductor junctions. This is because InAs has no Schottky barrier with metal when it forms a junction. However, the conventional shadow evaporation technique with PMMA as a top layer and a copolimer PMMA-MMA as a bottom layer does not work for fabricating the refractory metals such as niobium or tungsten. The problem is refractroy metals usually need an high evaporation temperature and ultra high vacuum to process it. This brings about the mechanical instability of the conventional resists during the evaporation of the refractory metals. The resulting out-gasing of the resist and consequent contamination degrade the electronic properties of deposited metal [68]. Various methods have been attempted to improve the shadow evaporation technique with more stable resists and mask structures [69, 68]. We tried a PMMA-Ge-PMGI tri-layer resist system to fabricate Nb film. We were able to have the Nb film of $T_c \gtrsim 8K$ for the wire width of $1\mu$m or wider. The thickness of Nb was 80 nm. This tells that the method we tried can be applied to fabricate Nb film. However, all the 2DEG sample with side contact to the Nb was made from our strong collaborator at BRL-NTT in Japan because they experienced to fabricate this high quality S-N hybrid system for many years. Niobium has a critical temperature of $\sim$ 9.3 K and critical field $\sim$ 2 T at 0 K in Bulk[70]. The energy gap of niobium $\Delta(0)/k_B T_c = 1.9$ which is experimentally deduced [70], is not far from the BCS value (1.76). The superconducting transition of the Nb film was tested via two contacts bonded to the Nb electrode. The transition temperature $T_c$ of the film was measured to be 8.5 K (See Figure 3.8). A suppression of $T_c$ in a film from its bulk value of 9.3 K is commonly observed, as is a similar suppression of $T_c$ in micro-fabricated structures. The relative modest suppression of $\approx 1$ K is in agreement with previous work, see for example [71].

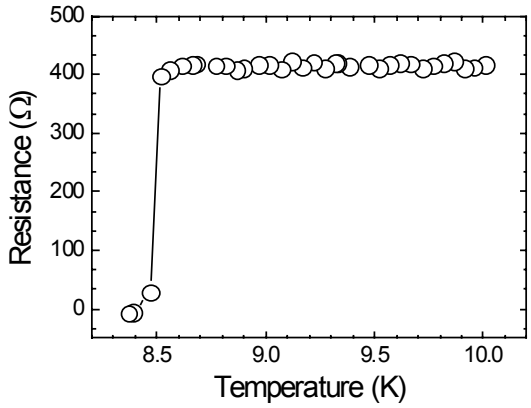


**Figure 3.8**: The superconducting transition temperature of the niobium measured with two probes on a structured device. It shows $T_c \sim 8.5$ K

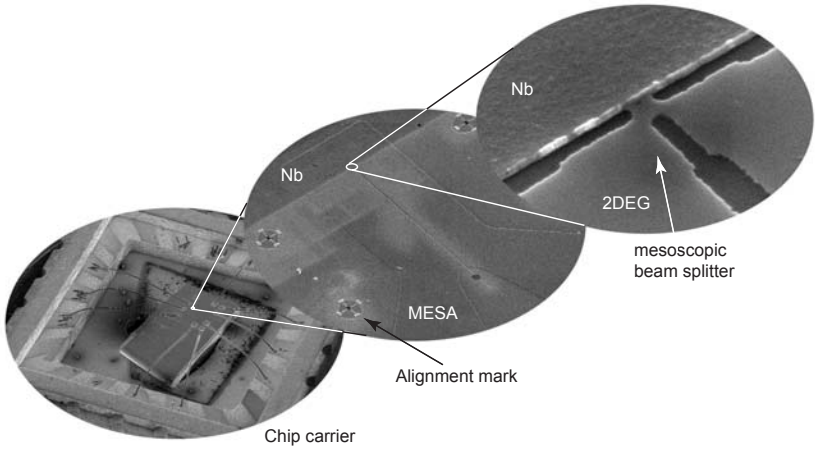


**Figure 3.9**: The overview of the real sample. From the lower left to the right : The device glued in a chip carrier and ready for the measurement. The MESA area in 2DEG and Nb contact. The final view of a sub-micron beam splitter geometry.

### 3.2.4 Bonding and final

The sample fabricated up to now need to be connected itself to the measurement equipment for performing the experiment. For this, we have an Ohmic contact on the sample as a bridge between mesoscopic device and macroscopic measurement setup.

The final step for the device to be ready for measurement is to connect the sample to the chip-carrier then the chip-carrier is further connected to the measurement setup. The sample substrate is glued into a chip-carrier with Epoxy and we connect the chip-carrier to the ohmic contact on the substrate using ultrasonic bonding machine with a 50-micrometer thick aluminium wire. When the sample is in the chip-carrier, we can mount it in the chip-carrier socket of one of the cryogenic systems for the measurement. Fig. 3.10 shows a sample after all the fabrication process and ready for the measurement.

## 3.3 Characterization of the sample

### 3.3.1 InAs 2-dimensional electron gas (2DEG)

When the sample is ready for the measurement, we first, check the device at room temperature using the R.T Box before real measurement at low temperature using the cryogenic systems. We check the ohmic contact of the 2DEG device at room temperature and the 4.2 K using the dip stick in the liquid helium dewar as we described in sec.3.2.1. When it shows normal value for the Ohmic resistance and the

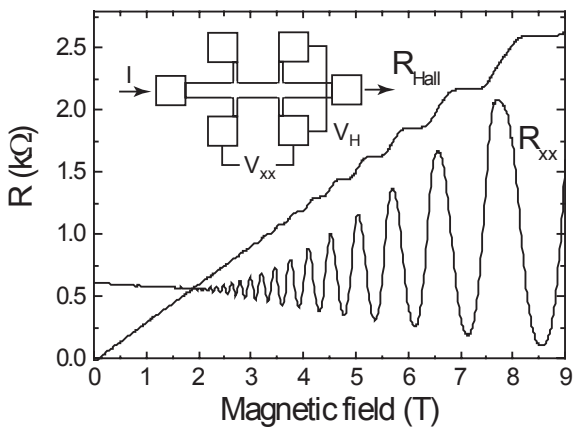


**Figure 3.10**: QHE measurement of InAs 2DEG system. inset: typical Hall bar geometry for QHE measurement.

resistivity, we continue the characterization of our 2DEG using Hall and Shubnikov-deHaas (or SdH) measurement in order to deduce the carrier density $n_s$ and the mobility $\mu$ individually.

Hall measurement is one of the basic characterization tool for the semiconductor 2DEG system because we can obtain the carrier density $n_s$ and the mobility $\mu$ individually from the measured resistivities $\rho_{xx}$ and $\rho_{yx}$. At a low magnetic field, the longitudinal resistance is constant while the Hall resistance increases linearly with magnetic field in agreement with semiclassical Drude model. From the low-field resistivities, we obtain the carrier density $n_s$ and the mobility $\mu$ as follows;

$$n_s = \frac{dB}{|e| d\rho_{yx}} = \frac{I/|e|}{dV_H/dB} \tag{3.1}$$

$$\mu = \frac{1}{|e| n_s \rho_{xx}} = \frac{I/|e|}{n_s V_{xx} W/L}\,. \tag{3.2}$$

Alternative to the Hall measurement, there is another simpler way to determine the characteristics of the semiconductor 2DEG called "van der Pauw" method [72]. Due to its' convenience, the Van der pauw method is widely used in the semiconductor industry to determine the resistivity of uniform samples. According to the original paper by van der Pauw, one can use arbitrarily shaped specimen without holes nor nonconducting islands or inclusions and thin-plate sample containing four very small ohmic contacts placed on the periphery (preferably in the corners) of the plate. A schematic of a rectangular van der Pauw configuration is shown in Fig.3.11. The current is forced one edge while the voltage drop is measured in the opposite edge. By shifting the role of the contacts by 90° and inverting the current direction,

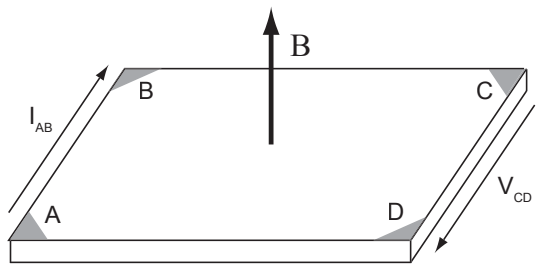


**Figure 3.11**: Schematic of a rectangular van der Pauw sample to determine the resistivity.

irregularities in the current flow can be ruled out. Taking the mean value of both measurements and weighting this with a characteristic function $f$, yields

$$\rho_{xx} = \frac{\pi d}{\ln 2} \frac{R_{\mathrm{AB,CD}} + R_{\mathrm{BC,DA}}}{2} f\Big(\frac{R_{\mathrm{AB,CD}}}{R_{\mathrm{BC,DA}}}\Big) . \tag{3.3}$$

Where, $d$ is the thickness of the lamella. The weighting function $f$ can only be expressed in the implicit form

$$\cosh\Big[\frac{R_{\mathrm{AB,CD}} - R_{\mathrm{BC,DA}}}{R_{\mathrm{AB,CD}} + R_{\mathrm{BC,DA}}}\Big] = \frac{1}{2} \exp \frac{\ln 2}{f} . \tag{3.4}$$

We can calculate $f$ numerically and it does not deviate much from the unity unless the measured resistances differ strongly from each other.

However, at high magnetic field, the measurements above are not valid anymore. This is due to the so called 'Landau quantization'[6]. In the Hall bar geometry, there are pronounced oscillations in the longitudinal resistance which are called Shubnikov-deHaas (or SdH) oscillations and the plateaus are appear in the Hall resistance corresponding to the every minimum in the longitudinal resistivity. This quantized Hall effect is known as quantum Hall effect (QHE) and first demonstrated by von Klitzing et.al [73].

Experimental work of QHE can be done by preparing a rectangular sample and measuring the longitudinal and transverse resistance of the sample. The inset in the Fig. 3.10. shows a schematic diagram of a typical 2DEG sample used for QHE measurement. From SdH oscillations, we obtain the carrier density $n_s$ by

$$n_s = \frac{2e}{h} \frac{1}{(1/B_1) - (1/B_2)} . \tag{3.5}$$

Where $B_1$ and $B_2$ are the magnetic field values for corresponding to two successive peaks. We choose many different values of $B_1$ and $B_2$ and plot the positions of the

[6]Quantized Hall effect is a subtle phenomenon and to explain this is beyond the scope of this work. We rather focus on practical use of QHE to characterize the semiconductor 2DEG.

maxima in $R_{xx}$ as a function of $1/B$ then, they lie in a strait line and the slope of the line yields the electron density $n_s$ [74].

# Chapter 4

# *Measurement setup*

## 4.1 Low temperature measurement

Most of the quantum effects in mesoscopic system require a low temperature of the order of a few Kelvin(K) or lower to be detected. In today's laboratory in condensed matter physics experiment, one uses cryo-liquids to cool down the samples. Typically liquid nitrogen $N_2$ which has the boiling temperature of 77 K is used to pre-cool the cryostat or to keep the cooling of the outer jacket of the cryostat to minimize the heat transfer through the radiation shield resulting the evaporation of the liquid helium in helium bath. Using the liquid helium dewar, one can reach 4.2 K which is the boiling point of $^4$He at the pressure of 1 bar. It can be further cooled down by pumping on the vapor above the liquid because the vapor pressure decreases roughly exponentially with decreasing temperature [75]. However, there is a limit for the minimum reachable temperature by pumping on a bath of the cryoliquids and the practical low temperature limits are 1.3 K for $^4$He and 0.3 K for $^3$He (See Fig. 4.1 ). The $^3$He-$^4$He dilution refrigeration method using a mixture of two helium isotopes can achieve the minimum temperature of $\sim$ 15 mK. During this thesis work, $^4$He and $^3$He-system from Cryogenics Ltd. have been used with the base temperatures of 1.7 K and 280 mK respectively.

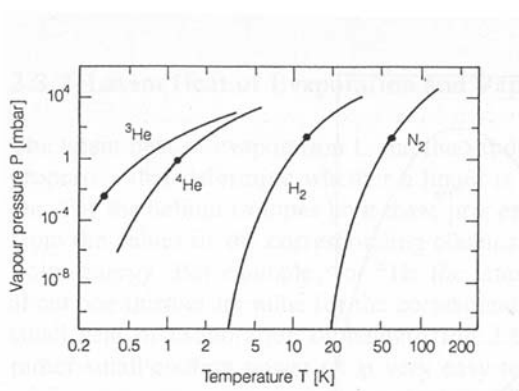


**Figure 4.1**: Vapor pressure of well known cryoliqids. The dots in the lines shows the practical limit for the low temperatures obtainable by reducing the vapor pressure of the cryoliquids. Picture taken from Ref. [75].

## 4.2 Noise measurement

Figure 4.2 shows the experimental setup for the typical conductance and noise measurements. For both measurements, the sample is DC-current biased through an high ohmic bias resistance $R_B \gg R_{sample}$ in series with the measured sample. $R_B$ is thermally anchored at the the bottom of 1 K - pot in order to minimize the thermal noise of the bias resistance itself. All the measurement lines are filtered at low temperatures by lossy microcoax cables. At the top of the cryostat, additional $\pi$-filters are used for RF-filtering of all the wires at room temperature. However, the leads for the detecting the fluctuations are filtered only at low temperature. Short SMA cables are used to connect between the top of the cryostat and the input of the LI75 amplifiers directly. We used two voltage sources for feeding the AC and DC bias to the sample. An Hewlett Packard 3245A voltage source produces the DC bias and Stanford Research DS360 function generator provides an AC current($f$ < 100Hz). These two currents are coupled by a passive 1:4 transformer whose ground is decoupled from the ground current of the rest of the circuit and used to determine the differential resistance of the sample. Two ultra-low noise amplifiers (LI-75, NF cor-

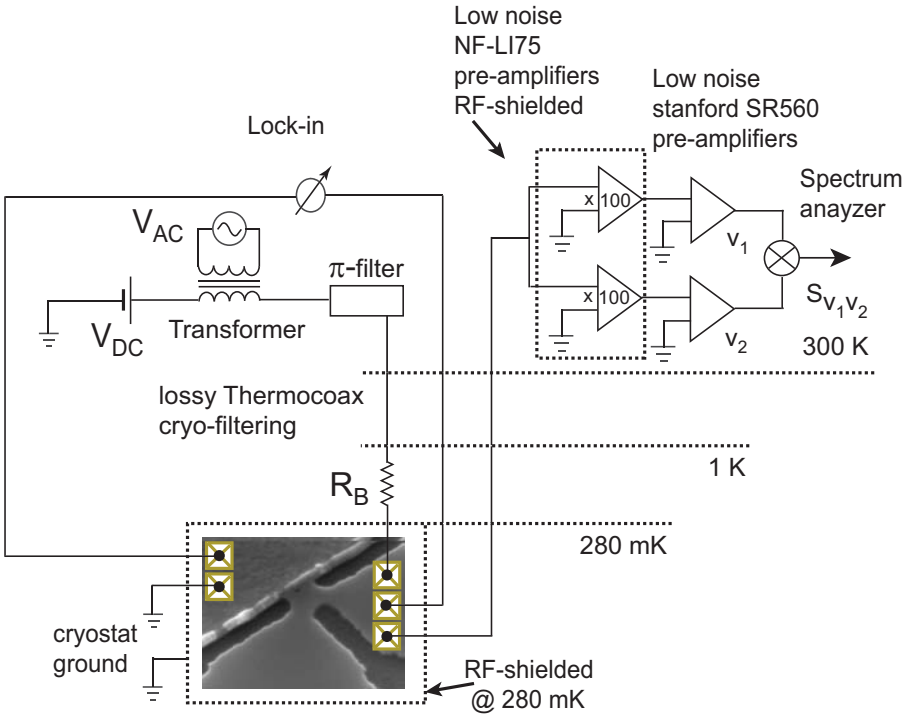


**Figure 4.2**: The schematic of the noise measurement setup consisting low temperature filtering with thermocoax cables and $\pi$-filters at room temperature. The differential resistance of the sample was measured using Lock-in technique. See text for the explanation.

poration with fixed gain 100) followed by two low-noise amplifiers (Stanford SR560) are used to measure the voltage fluctuations across the sample. All amplifiers are powered by independent sets of batteries to avoid cross talk. The voltage signals from the amplifiers are cross-correlated (See Figure 4.3b) and fed into a spectrum analyzer HP 89410A which performs a fast Fourier transformation of the two output voltage signals $V_1$, $V_2$ and a vector averaging over successive temporal traces. The cross-correlation technique[76], as we will show in next section, eliminates the voltage noise contributions of the measurement setup. A typical noise measurement was done in the frequency range between 30 and 200 kHz and the resistance of the sample was about 2k$\Omega$. The spectra were measured over 401/802 points and averaged 500 times or more depending on the spectrum range. However, in order to avoid $1/f$-noise at higher bias currents, most of the reasonable spectra were taken at the frequency of $\sim$ 100 kHz or higher. At this frequency range, there is a RC-damping in the measurement circuit to the measured signals and we need to calibrate the measured data to deduce the correct value. We will discuss about the data calibration in next section.

### 4.2.1 Low frequency noise detection scheme

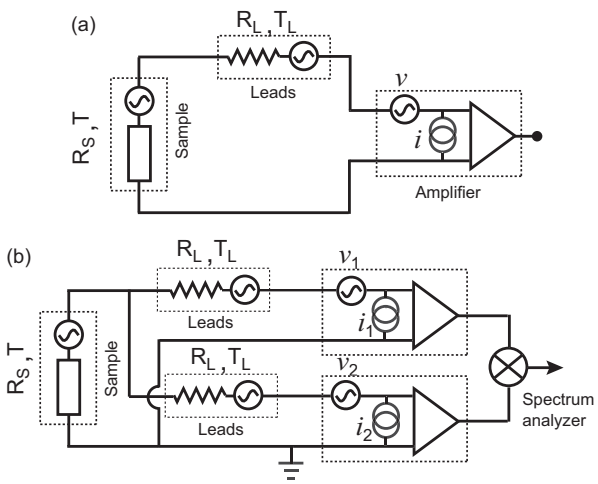


**Figure 4.3**: (a) Conventional way of noise detection circuit with one amplifier. (b) Cross-correlation technique, analogous to the four-point method in resistance measurements with two amplifiers in parallel.

Before continue to characterize our measurement setup, we would like to describe the cross-correlation technique known as a reliable and sensitive way to detect the low frequency noise of the device [76]. From the Fig.4.3a, we denote $R_S$ as a resistance of the sample at temperature T, $R_L$ is the resistance of the leads at temperature $T_L$, and $v$ and $i$ are the voltage and current noise of the amplifier respectively. The

conventional way to detect the voltage noise fluctuation $\langle V^2 \rangle$ across the sample is to send the output of a low-noise voltage amplifier to a fast Fourier transform spectrum analyzer, which gives the spectral density of the total voltage noise in a bandwidth $\Delta f$. Then the square of the total voltage noise is

$$\langle V^2 \rangle = \langle V_S^2 \rangle + (R_S + R_L)^2 i^2 + v_0^2(1 + f_1/f) + 4k_B T R_L \Delta f \,. \tag{4.1}$$

where we have written $v^2 = v_0^2(1 + f_1/f)$ to emphasize the $1/f$ voltage noise of the amplifier below a characteristic frequency $f_1$. From the above expression, we see that the determination of the sample noise requires the knowledge of the noise characteristics of the amplifier $(v, i, f_1)$ and of the temperature and resistance of the leads. We can use a correlation method shown in Fig.4.3b which is analogous to the four-point method used to measure a resistance. Here, by measuring the voltage noise with two independent amplifiers in parallel and multiplying the output, the voltage noise contribution of the leads and the amplifiers is eliminated (See Fig.4.7 for the comparison of these two methods). The cross-correlation spectral density of the two output voltage of amplifier 1 and 2 is, referenced to the input

$$\langle V_1 V_2 \rangle = \langle V_S^2 \rangle + R_S(R_S + R_L) i_1^2 + R_S(R_S + R_L) i_2^2 \tag{4.2}$$

$$= \langle V_S^2 \rangle + 2R_S^2 \cdot i_{Amp}^2 \,. \tag{4.3}$$

for $R_L << R_S$. Where $i_{Amp}^2 = i_1 = i_2$ represents the current noise of the amplifier. Thus, the determination of the sample noise requires only the knowledge of the spectral density of the current noise of the amplifiers.

### 4.2.2 Characterization of the noise-measurement setup

As we mentioned in earlier section, there is a $RC$-damping of the measured signal because the whole measurement setup behaves like a $RC$-filter with the total resistance $R$ and the total capacitance $C$ of all the measurement lines and amplifiers. This attenuation can be calibrated by measuring the equilibrium voltage noise $S_V = 4k_B RT$ as a function of temperature $T$, as shown in Fig. 4.4a. where, $k_B$ is the Boltzmann constance and $R$ is the sample resistance. The calibration has been checked for different frequencies and sample resistances (Fig.4.4b). However, it is necessary to know in detail about the characteristics of the measurement setup to do correct data analysis on the measured data. For characterizing the measurement setup, we introduce an electric circuit model contains a RC-filter based on the discussions above. In Fig.4.5, simplified model of the measurement setup for the noise detection is shown. From this model, we can calculate the output voltages, the transfer function and finally the cross-correlation of two output voltages of the circuit. The resistance of the bias line is dominated by bias resistance $R_B$ and the capacitance of the bias line is mainly due to the capacitance of thermocoax cable at low temperature. Therefore only one capacitance $C_B$ represent the bias line capacitances. $R_L$ and $C_L$ represent the resistance and the capacitance of all the noise

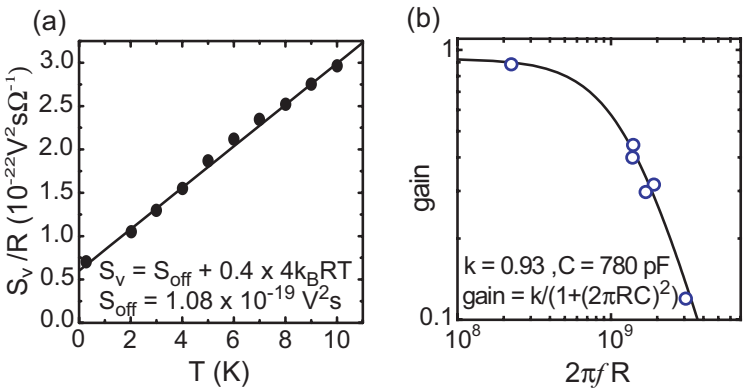


**Figure 4.4**: (a) measured data of equilibrium(Thermal) noise versus sample temperature for the calibration of data. Thermal noise is linearly proportional to the temperature and the slope of the plot gives the attenuation factor of the signal. It shows $\sim 0.4$ for $f = 100$ kHz with $f$ the center of the frequency window. (b) RC-damping of the signal for different frequencies and sample resistances. Solid curve presents a theoretical fit from the data and yields a total capacitance of the measurement setup about 780 $pF$.

detecting lines including the amplifiers. The noise introduced by $R_L$ is negligible compared to the other noise sources thus, it is not taken into account. The exact expression of the output voltage $V_1$ and $V_2$ is quite complicated for all the resistance and the capacitance terms in this model. However, we know from the measurement that the bias resistance $R_B$ and the sample resistance $R_S$ are much bigger than the resistance of the leads $R_L$ i.e., $R_L/R_B \ll 1$, $R_L/R_S \ll 1$, thus in the low frequency limit, the term $\omega R_L C_L$ is negligible. We further simplify that the capacitance of whole circuit is represented by single total capacitance $C_{tot} = C_B + 2C_L$. Neglecting all the smaller terms, we can get relatively simple expressions for the two out put voltages $V_1$ and $V_2$ [1]:

$$V_1 = \frac{R_S(i_B + i + i_1 + i_2)}{1 + (R_S/R_B) + j\omega C_{tot} R_S} + R_L i_1 + v_1 \tag{4.4}$$

$$V_2 = \frac{R_S(i_B + i + i_1 + i_2)}{1 + (R_S/R_B) + j\omega C_{tot} R_S} + R_L i_2 + v_2 \,. \tag{4.5}$$

where $i_B, i, i_1, i_2$ are four current noise source terms from bias resistance, sample and two amplifiers respectively. $v_1$ and $v_2$ are two voltage noise sources from the amplifiers. Here, only the fluctuating part is present and all the D.C. part is ignored. After the average of the cross correlation of the two output voltages $\overline{V_1}\, V_2$, the terms which do not have a constant phase relationship between them will be eliminated. Consequently, the contributions of the voltage noise sources of the amplifiers and

[1] We will show in the appendix A more rigorous expression for $V_1$ and $V_2$ and in the limit case with the conditions above, it recovers the same expression as Eqn. 4.8

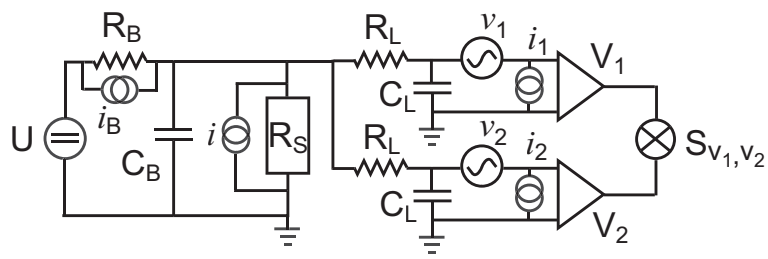


**Figure 4.5**: The electric circuit model of the measurement setup. U is the DC-bias source and from the bias lines, the bias resistance $R_B$ is dominant and its' current noise source $i_B$, the $C_B$ represents the capacitances of the bias lines. $R_S = dV/dI$ is the differential resistance of the sample and it is important to denote as a differential resistance because of it's non-linearity. $i$ is the current noise source of the sample which we are interested to measure. $R_L$ and $C_L$ are the total resistance and capacitances of the measurement lines including the amplifiers respectively. $i_1, i_2$ and $v_1, v_2$ are the current and voltage noise sources of the amplifires and the measurement lines.

the measurement lines which contains $1/f$ component are averaged to zero (See Sec.4.2.1 or Ref. [76] for details and See Fig. 4.7 for a practical example.) and only terms like $\langle \overline{x} \cdot x \rangle$ remain in the expression. Hence, the cross-correlation $\langle \overline{V_1} \cdot V_2 \rangle$ is just:

$$\begin{aligned} S_{V_1,V_2} &= \langle \overline{V_1} \cdot V_2 \rangle = \frac{R_\parallel^2}{1+(\omega C_{tot} R_\parallel)^2}\Big(\langle \overline{i_B} \cdot i_B \rangle + \langle \overline{i} \cdot i \rangle + \langle \overline{i_1} \cdot i_1 \rangle + \langle \overline{i_2} \cdot i_2 \rangle\Big) \\ &+ \frac{R_\parallel R_L}{1-j\omega C_{tot} R_\parallel}\Big(\langle \overline{i_2} \cdot i_2 \rangle\Big) + \frac{R_\parallel R_L}{1+j\omega C_{tot} R_\parallel}\Big(\langle \overline{i_1} \cdot i_1 \rangle\Big) \qquad (4.6) \\ &= \frac{R_\parallel^2}{1+(\omega C_{tot} R_\parallel)^2}\Big(S_B + S_I + 2\Big[1+\frac{R_L}{R_\parallel}\Big]S_{Amp}\Big). \qquad (4.7) \end{aligned}$$

here we denote the parallel resistance of $R_B$ and $R_S$, i.e., $R_\parallel = R_B R_S/(R_B + R_S)$ and $S_B = \langle \overline{i_B} \cdot i_B \rangle, S_I = \langle \overline{i} \cdot i \rangle$, $S_{Amp} = \langle \overline{i_1} \cdot i_1 \rangle = \langle \overline{i_2} \cdot i_2 \rangle$. This simplified expression remains true for the relevant parameters of the contact resistances and the frequency range for our experimental setup. So, the DC bias dependent power spectrum of the current fluctuations of the sample can be extracted from the measured cross-correlation spectrum $S_{V_1,V_2}$ as follows:

$$S_I = \frac{1+(\omega C_{tot} R_\parallel)^2}{R_\parallel^2} S_{V_1,V_2} - S_B - 2\Big(1+\frac{R_L}{R_\parallel}\Big)S_{Amp} \qquad (4.8)$$

Where the prefactor $(1+(\omega C_{tot} R_\parallel)^2)/R_\parallel^2$ indicates the resulting attenuation of the measured signal from this RC-circuit model and the determination of these factors is described in Appendix.A. Figure 4.6 shows an example of the measured raw data of cross-correlation spectrum $S_{V_1,V_2}$ for a wide frequency window. Each spectrum

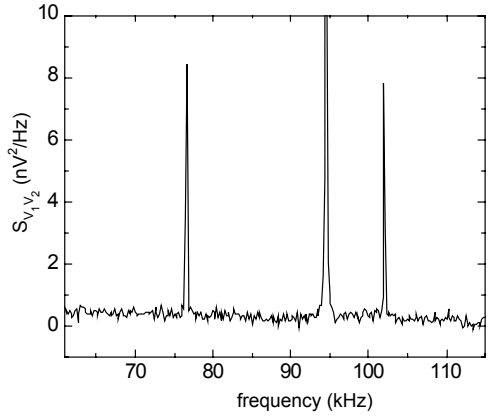


**Figure 4.6**: Typical raw cross-correlation power spectrum of the voltage fluctuation of the sample. We tried to measure the noise in a chosen frequency window which there are no spikes exist for example, between 80 and 90 kHz in this case.

consist of 401/802 points distributed over the chosen frequency window. We try to choose the frequency window where there is no spikes or the minimum number of spikes as possible. Then the measurement program calculates the average noise power of the averaged spectra excluding the points which are off from the average by a certain magnitude which can be manually set. There is another method for obtaining the average noise power which uses the mean value of the Gaussian fit of the spectrum. This alternative method is less sensitive to the peaks in the spectrum and allows one to use a large frequency window so that the averaging time is reduced.

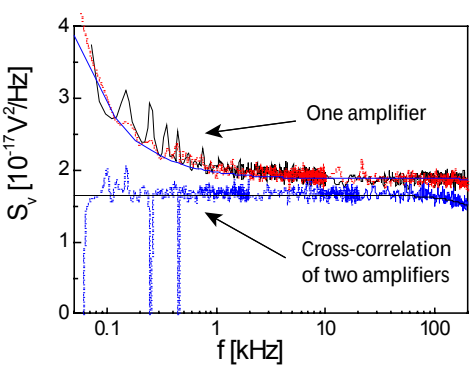


**Figure 4.7**: An example of the $1/f$ noise suppression in cross-correlation scheme. The spectrum density from one amplifier has a substantial $1/f$ noise up to few $kHz$. However, cross-correlation technique with two amplifiers in parallel eliminates $1/f$ part considerably.

**Table 4.1**: Summary of measured parameters.

| Parameter | Value |
|---|---|
| Bias resistance $R_B$ | 1.037 MΩ |
| Noise of Bias resistance $S_B$ | $1 \times 10^{-28} A^2 s$ |
| Total capacitance $C_{tot}$ | 780 pF |
| Measurement line resistance $R_L$ | $\sim 30\Omega$ |
| Current noise of the NF-preamplifier $S_{Amp}$ | $5 \times 10^{-28} A^2 s$ |

## 4.3 Gating of the InAs heterostructures

### Motivation

The idea is to separate the spin singlet Cooper pairs of electrons spatially with a Y-shaped 'beam splitter' on the normal side. Measurements of the cross-correlations of the current noise in the two arms, can reveal whether a separation of the Copper pairs is achieved or not. This is very important in order to demonstrate spin entanglement of electrons in the vicinity of a normal-superconducting interface which can be our long-term aim from this device. The ability to tune the device with gates is desirable for a number of reasons.

- It will be an advantage to be able to tune the electron densities in the two arms separately, to ensure that orbital energies are the same. Further more, if the positive correlation in the noise is a mesoscopic effect, as it was suggested in Ref.[77], then a tuning of the devices is necessary.
- A theoretical suggestion to ensure the spatial separation of the Cooper pair is to place quantum dots in each arm [27]. Quantum dot engineering needs gates that can actually deplete the electron gas.
- Measurements of a positive current noise correlation of the two electron beams cannot prove entanglement. To do this, on would for instance need to tune the spins in the two beams independently. This might be done using the Rashba effect, with gates to produce an electric field.

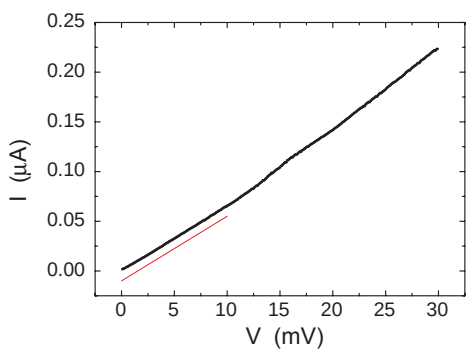


**Figure 4.8**: I-V curve of connection between a Ti/Au topgate, and a InAs mesa. There is a linear behavoir with a resistance of 150 kΩ.

### Test of gated device[2]

The presented samples are made on the InAs wafer without any superconducting Nb contacts. Gating of InAs heterostructures is made difficult by the fact that InAs

[2]Note that this test was done before we found out the right parameters for the annealing process so all the 2DEG behaviors are much resistive than it should be. Refer the sub-section 3.2.1 for the details.

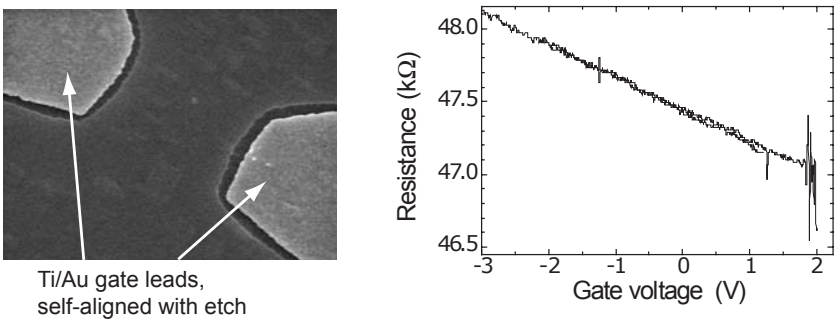


**Figure 4.9**: Left: SEM picture of a 4 $\mu$m wide etched opening with metal side gates, Right: Resistance of a sample similar to the Figure in left, as function of the voltage applied to the gates. Two sweeps shown. At 2 V fluctuations appear due to a large leak current.

has no native Schottky barrier. This is illustrated by the results of a test experiment shown in Fig.4.8. A 20$\mu$m wide Ti/Au top-gate has been deposited across a 50$\mu$m wide etched-out mesa, with ohmic contacts. The I-V characteristic from the top-gate to the InAs 2DEG shows a linear dependence, with a resistance of 150 k$\Omega$ , probably due to leakage from the side-walls of the mesa. To separate the gate from the 2DEG, we created an in-plane self-aligned side gate. See Fig.4.9. An opening was wet-etched out in the mesa, and the protective layer of PMMA resist was used as a lift-off mask for a subsequently deposited Ti/Au top gate. For details of the fabrication procedure, see in Appendix B. Undercut of the resist, and undercut by the wet-etch, results in a 100-500 nm separation of the gate from the un-etched mesa.

Measurements of the gate effect on a similar sample, where the gates are 3$\mu$m apart, are shown in Fig.4.9 The 2-terminal resistance is measured between ohmic contacts at each end of the 300 $\mu$m long and 50 $\mu$m wide mesa. If the gate voltage is increased above +1 V or below -1 V, the leak current from the gates to the 2DEG starts to increase above the noise level of 50 pA for this measurement. In this gate voltage window, the resistance of the sample changes with less than 0.5 k$\Omega$.

As a further refinement of the gating technique, we pre-etched parts of the mesa. This had the effect of separating the gate electrode further from the InAs, and thus reducing the probability of leak currents. The resulting sample can be seen in Fig.4.10. Only near the constriction is the gate-InAs lateral separation defined by the self-alignment technique, here resulting in a separation of 200 nm. In the left of the Fig.4.11, the effect of the gate voltage on the resistance of the constriction can be seen. The gate can be biased from -2 V to +2.5 V without any detectable leak current (Right in Fig.4.11). In this gate voltage interval, the resistance of the junction changes by less than 0.3 k$\Omega$.

As a further demonstration of the resistive decoupling of the gate and the 2DEG, we show in Fig.4.12 current-voltage characteristics from the gates to the 2DEG. We

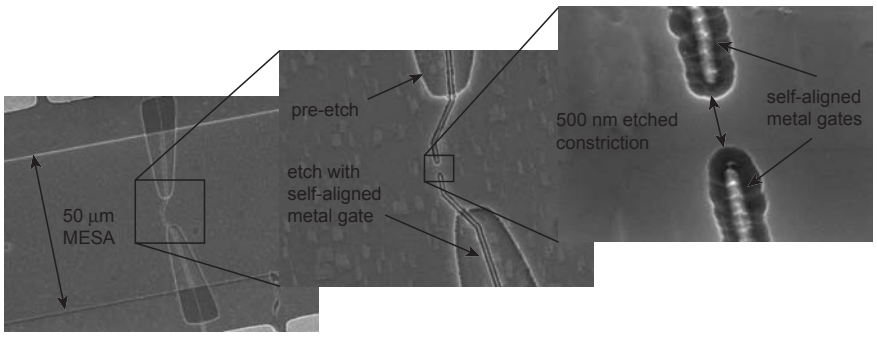


**Figure 4.10**: SEM picture of the sample geometry. A constriction is defined in two steps on a 50 $\mu$m wide mesa, see text for the explanation.

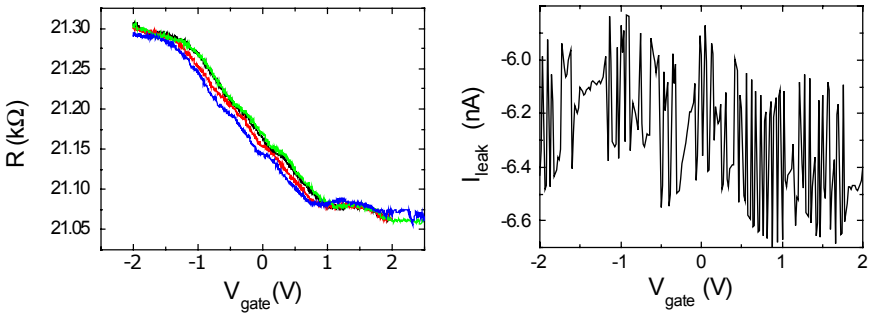


**Figure 4.11**: Left: Resistance of the sample in Figure 4.10, as function of gate voltage. Several gate sweeps shows some reproducability. If the applied gate voltage is taken to higher or smaller values, the resistance start to fluctuate and reproducability is lost. Right: Leak DC current of the sample in Figure 4.10 (there is an arbitrary offset). The resistance shown in left figure is measured by applying an AC current.

conclude that there is a resistance of the order of $1/G$(Quantum conductance) from the gates to the 2DEG.

All measurements presented were done at a temperature of 5.2 K, using voltage biased AC lock-in methods (frequency 27 Hz, RMS bias voltage 0.5 mV) to measure the resistances.

### Conclusion

By separating metallic side-gates 100-200 nm from the InAs heterostructure, we have achieved very high gate-2DEG resistance, and hence small leak currents, for gate biases of a few Volt. On the other hand, the gate efficiency has shown to be very poor. It seems unlikely, that this gating technique can be used to effectively tune the Y-branch, even though there is still some room for improvement of the technique (by for instance make the constrictions narrower). Further, if this method

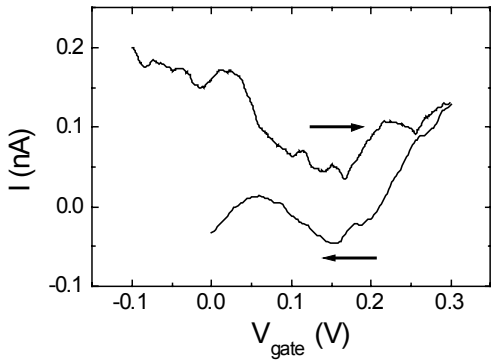


**Figure 4.12**: I-V characteristic of gate-2DEG for one of the gates of the sample in Figure 4.10. The other gate shows similar characteristics. The fluctuations are not reproducible, and no linear behavior is seen.

should be used to control tunnel junctions leading to a quantum dot, then one has to be able to deplete the electron gas. On the basis of the present measurements, it seems not possible to achieve this.

# Chapter 5

# *Shot noise in superconductor-semiconductor heterostructure junction*

## 5.1 Introduction

Shot-noise measurements provide a powerful tool to study charge transport in mesoscopic systems.[1] Whereas resistance measurements yield information on the average probability for the transmission of electrons from source to drain, shot-noise provides additional information on the electron transfer process, which can not be obtained from resistance measurements. For instance, the charge of the quasi-particles can be extracted from shot-noise measurements, an experiment that was applied to the fractional quantum Hall regime.[3, 4, 5] Shot-noise also provides information on the statistics of the electron transfer. In general, the fermionic nature of the particles lead to a suppression of the shot-noise from its classical value $S_I = 2e|I|$, corresponding to Poissonian statistics ($S_I$ is the power-spectral density of current fluctuations in units of $A^2$s). Suppression can also be induced by Coulomb interaction, which was observed in the single-electron tunneling regime.[48] That shot-noise can be fully suppressed in an open channel was confirmed in quantum-point contacts.[78, 79] In a general conductor, the suppression is not full, but depends on the actual distribution of transmission eigenvalues.[57, 80, 81] For example, shot-noise is suppressed to 1/3 in a disorder wire [9, 10, 11, 12, 13, 14] and to 1/4 in an open cavity.[15, 82, 16, 17] For a recent review, see Ref. [83].

Different to mesoscopic devices with normal electron reservoirs, shot-noise can be enhanced in devices with superconducting leads by virtue of the Andreev reflection process taking place at the interface between a normal metal and a superconductor.[84, 18, 71, 85, 6, 86, 87] In some limiting cases, e.g. in the tunnelling and disordered limit, the shot-noise can be doubled with respect to its normal state value.[57, 51, 88, 19, 20, 21]

In addition to measure shot-noise in a two-terminal geometry, multi-terminal fluctuation measurements have been proposed.[22] Whereas shot-noise corresponds

to the autocorrelation of fluctuations, cross-correlation measurements of fluctuations between different leads provide a wealth of new experiments. As pointed out by Büttiker, exchange-correlations can for example be measured directly.[22] In an attempt to go beyond conventional shot-noise measurements, correlation measurements [14, 23] on electron beam-splitters [24] were studied. The partitioning of a 'stream' of ferminons in a beam-splitter results in negative correlations between the fluctuations measured on the two output ports (anti-bunching). In contrast, bunching-like behavior (positive correlation) has theoretically been predicted in multiterminal devices in which at least one electrode is a superconductor.[59, 61, 40, 62] In the subgap region, charge is injected from the superconducting lead into the device in correlated pairs of electrons, which - in the simplest picture - may separate in the normal scattering region and exit at two different leads. As a consequence, the current in the exit leads fluctuate in parallel. However, it has been pointed out, that this picture is misleading, in particular in the regime where the superconductor is strongly coupled to the normal region. In this case, the normal region should rather be viewed as a proximity-induced superconductor.[89] Positive correlations have not been observed in mesoscopic devices until today.

Finally, we mention that the experimental quest for positive correlations is also important for the new field of quantum computation and communication in the solid state, [31, 32] in which entangled electrons play a crucial role. A natural source of entanglement is found in superconductors in which electrons are paired in a spin-singlet state. A source of entangled electrons may therefore be based on a superconducting injector.[33, 34, 27, 35, 36, 37, 38, 39, 40, 41] Even more so, an electronic beam-splitter is capable of distinguishing entangled electrons from single electrons.[29, 42]

We have therefore focused our experimental research on the fabrication of superconducting injectors (Nb) into a high-mobility InAs-based two-dimensional electron gas (2DEG),[90, 91, 92, 93] in which beam-splitters can be fabricated. In this article, we focus on the fabrication of such devices in Sec. 5.2 and their characterization in terms of linear and non-linear resistance in Sec. 5.3.1, as well as shot-noise in Sec. 5.3.2. Near the superconductor-2DEG interface two etched sub-micrometer constrictions define a beam-splitter which divides the input current. We study the shot-noise of the current from the superconductor to one of the normal reservoirs and observe an enhancement for bias currents corresponding to voltages below the superconducting gap of the Nb contact. This enhancement is due to Andreev reflections at the superconducting contact and disappears in a magnetic field higher than the critical field of Nb. Using the coherent scattering theory, we extensively compare our measurements with different models in Sec. 5.4. Our devices can best be described as composed of a highly transparent S-N interface in series with a short scattering region, whose size $L$ is comparable to the elastic mean-free path $l_e$. It may therefore be named a quasi-ballistic S-N beam-splitter junction.

## 5.2 Experiment

The InAlAs/InGaAs heterostructure was grown by molecular beam epitaxy on a Fe-doped semi-insulating InP substrate. The 2DEG is confined in a 4 nm wide InAs quantum well 35 nm below the surface of the heterostructure, see Ref. [90] and Fig. 5.1a for details. The substrate is first structured into a 50 $\mu$m wide Hall bar (MESA) by wet etching. Hall and Shubnikov-de Haas measurements (Fig. 5.1b) then yield an electron density of $n_e = 2.1 \cdot 10^{16}\,\mathrm{m}^{-2}$ and a mobility of $\mu = 5.0\ \mathrm{m}^2/\mathrm{Vs}$ for the 2DEG, corresponding to a Fermi wavelength of $\lambda_F = 18\,\mathrm{nm}$ and an elastic mean free path of $l_e = 1.2\,\mu\mathrm{m}$.

The Nb electrode is defined by electron beam lithography at one side of the MESA. First, the MESA is etched in the patterned electrode area to a depth of $\sim 50$ nm. Then, the sample is mounted in an evaporation chamber and rf-sputter cleaned. Without breaking the vacuum, a 80 nm thick Nb film is subsequently deposited at an angle of 30 degrees to the horizontal. After lift-off, a 50 $\mu$m wide superconductor-2DEG contact is obtained. A cross-section through such a Nb contact is schematically shown in Fig. 1a.

E-beam lithography is now used to reduce the macroscopic superconductor-2DEG contact to sub-micron dimensions, see Fig. 5.1c. This is achieved by etching

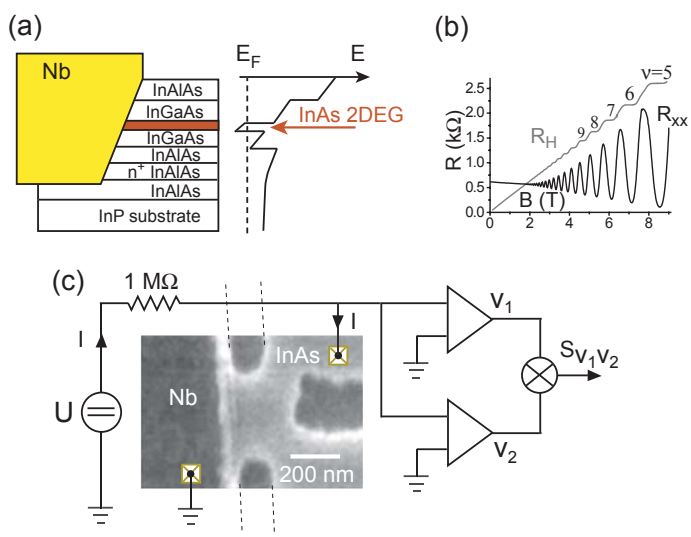


**Figure 5.1**: (a) Schematic side view of the Nb contact to the InAs semiconductor heterostructure and the corresponding energy band diagram. (b) Longitudinal ($R_{xx}$) and Hall ($R_H$) resistance measured on this heterostructure. (c) SEM picture of a sample (top view) with a diagram of the measurement setup. The sample is current biased through a series resistor and the voltage fluctuations are measured with the aid of two sets of amplifiers whose outputs are cross-correlated. $S$ denotes the power spectral density in units of $\mathrm{V}^2/\mathrm{Hz}$.

trenches into the heterostructure to a depth of 60 nm below the surface, removing the conducting InAs quantum well. Three trenches are etched, two vertical ones and one horizontal one, which start at the nanometer-sized contact in front of the superconductor and extend across the whole MESA. The vertical trenches have a width of about $\sim 100$ nm and are placed parallel and as close as possible to the Nb interface at a distance of less than 50 nm. The three-terminal junction consist thereafter of a $300 \times 350$ nm square area in the 2DEG which is bound on one side (350 nm wide) by the edge of the superconductor and the other side by two constrictions leading to two macroscopic normal electron reservoirs. The constrictions have a nominal width $w$ of 170 nm, corresponding to $N = 2w/\lambda_F \approx 19$ conducting channels. This part can be viewed as a beam-splitter for charge carriers (Cooper pairs in the superconducting state), injected from the Nb contact.

The sample is mounted in a $^3$He cryostat with a base temperature of 270 mK. Here, we restrict ourselves to two-terminal measurements as schematically shown in Fig. 5.1c. The sample is current biased through a 1 MΩ series resistor thermally anchored at the 1 K pot of the cryostat. The current is determined by the DC bias voltage $U$, on which a small AC voltage is superimposed in order to measure the differential resistance $dV/dI$. All measurement lines are filtered at low temperature by lossy microcoax cables and additional $\pi$-filters are used at room temperature. Two ultra-low noise amplifiers (LI-75, NF corporation) with a fixed gain of 100, followed by two low-noise amplifiers (Stanford SR560, operated at a nominal gain of 10 or 100), are used to measure the voltage fluctuations across the sample in parallel. All amplifiers are operated at room temperature and powered by independent sets of batteries to minimize cross-talk. The voltage signals from the amplifiers are then cross-correlated by a spectrum analyzer (HP 89410A). This cross-correlation technique [76] can eliminate (or greatly reduce) the voltage noise contributions due to the two amplifiers, because they ought to fluctuate in an uncorrelated manner.

In order to measure shot-noise, which is a frequency independent contribution, one has to ensure that $1/f$-noise can be neglected at the highest bias currents. As a consequence, we have measured the noise at rather large frequencies $f$ around $50 - 200$ kHz. In this window, $1/f$ noise can be neglected up to the highest currents of $\approx 2\,\mu$A. Due to capacitances in the whole circuit including the measurement lines, the signal is damped. The overall gain, including the frequency-dependent attenuation, has to be carefully calibrated for each device separately. This is done by measuring the equilibrium voltage noise (i.e. the thermal noise), given by $S_V = 4k_BTR$, as a function of temperature $T$, as shown in Fig. 5.2a. Here, $k_B$ is the Boltzmann constant and $R$ is the linear-response sample resistance (more precisely, the parallel connection of the sample resistance with the series biasing resistor). The measured voltage noise $S_{V_1,V_2}$, including the amplifier noise, can be written as (see Fig. 1c):

$$S_{V_1,V_2} = A(\omega)R^2(S_I + S_{I,\text{off}}) + S_{V,\text{off}} \tag{5.1}$$

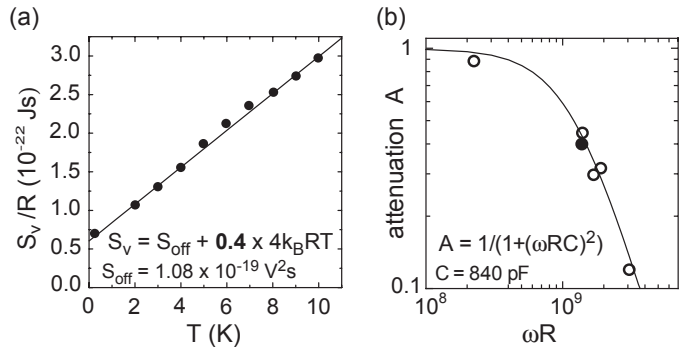


**Figure 5.2**: (a) Example of a measurement of the equilibrium (thermal) voltage noise (spectral density $S_V$) versus temperature $T$ used to deduce the calibration parameters. Here, the frequency and sample resistance were $f = 110\,\mathrm{kHz}$ and $R \backsimeq 2\,\mathrm{k\Omega}$, respectively. The thermal noise is linearly dependent on $T$ and the slope. For the calibration an average value for $R$ was used. yields the attenuation factor $A$ of the signal. (b) The attenuation $A$ as a function of $\omega R$ follows the dependence expected for a simple RC network, i.e. $A(\omega) = (1 + (\omega RC)^2)^{-1}$.

Here, $S_I$ is the current noise of the sample, which in the calibration procedure is of thermal origin only, i.e. $S_I = 4k_BT/R$. $S_{I,\mathrm{off}}$ denotes the current noise offset of the two LI-75 amplifiers. This contribution cannot be eliminated by the cross-correlation scheme. We also find a non-zero voltage noise offset $S_{V,\mathrm{off}}$ accounting for residual cross-talk between the amplifiers, possibly due to spurious ground currents. The nominal overall gain of either $10^3$ or $10^4$ of the amplifiers has been divided off in the above Eq. 5.1. Hence, all the quantities refer to 'input' noise. Finally, $A(\omega = 2\pi f)$ denotes the frequency-dependent attenuation factor.

A typical calibration measurement at $f = 110\,\mathrm{kHz}$ is shown in Fig. 5.2a. The attenuation $A$ at this frequency is obtained from the slope of $S_V(T)$ and the residual amplifier noise from the vertical offset of the fitted linear dependence extrapolated to $T = 0$.[1] The attenuation was measured for different devices with varying resistances $R$, ranging between $\approx 1.5$ and $\approx 2.5\,\mathrm{k\Omega}$ and frequencies in the range of 50 to $\approx 200\,\mathrm{kHz}$. $A(\omega)$ for a set of devices is shown in Fig. 2b to follow the expected damping for a simple RC network, i.e. $A(\omega) = (1 + (\omega RC)^2)^{-1}$. The extracted capacitance of $C = 840\,\mathrm{pF}$ is mainly due to the filtering of the wires (microcoax-filters) and the two input capacitances of the amplifiers.

The noise offset $S_{\mathrm{off}}$, extracted from the calibration procedure, typically amounts to $1 \cdot 10^{-19}\,\mathrm{V^2s}$. The current noise of a single LI-75 amplifier is specified to be $< 2 \cdot 10^{-28}$ $\mathrm{A^2s}$ and independently measured to be $< 8 \cdot 10^{-28}\,\mathrm{A^2s}$, corresponding

[1] The linear dependence of $S_V(T) - S_{V,\mathrm{off}}$ with temperature T which we used in the calibration is not exact, because $R$ is not constant but temperature dependent as well. $R$ varies in the temperature range by $\pm \approx 10$. For the calibration, average value for $R$ was used.

to a voltage noise of $< 3.2 \cdot 10^{-21}\,\mathrm{V^2s}$ for a single amplifier on a typical sample resistor of $R = 2\,\mathrm{k\Omega}$, or to $< 6.4 \cdot 10^{-21}\,\mathrm{V^2s}$ for two amplifiers in parallel. The offset current noise of the amplifiers is therefore at least an order of magnitude smaller than the measured offset and can therefore not account for it. Hence, the dominating part of the measured offset is caused by residual voltage fluctuations. The voltage noise floor of a single LI-75 amplifiers is specified to be $1.4 \cdot 10^{-18}\,\mathrm{V^2s}$ and independently measured (short circuit input) to be $2.5 \cdot 10^{-18}\,\mathrm{V^2s}$, a value which is substantially larger than the measured offset noise after the cross-correlation. The cross-correlation technique therefore reduces the voltage fluctuations of the amplifiers by as much as a factor of 25.

The deduced calibration parameters are then used to extract the intrinsic current shot-noise $S_I$ generated in a superconducting-2DEG junction from the measured noise $S_{V_1,V_2}$ using Eq. 5.1. It is important to emphasize, that $R$ in Eq. 5.1 has to be replaced by the differential resistance $dV/dI$ for the non-equilibrium measurement. This is crucial, because of the non-linear current-voltage characteristic of these devices.

## 5.3 Results

We measured the linear-response resistance $R$ as a function of temperature $T$, the differential resistance $dV/dI$ and the spectral density of the voltage fluctuations (the noise) as a function of bias current $I$, both at $T = 270\,\mathrm{mK}$. We focus first on the resistance and then on the noise measurements.

### 5.3.1 Resistance measurements

Fig. 5.3 shows the temperature dependence of the linear-response resistance $R$ measured from the superconductor to one of the normal reservoirs, as schematically shown in Fig. 5.1c. Above $T = 7.5\,\mathrm{K}$, the resistance is constant, whereas it varies non-monotonically below. $R$ first drops abruptly below $7.5\,\mathrm{K}$, has a minimum at $\approx 6\,\mathrm{K}$ and then starts to increase for lower temperatures. At the lowest temperature, $R$ is $\approx 8\,\%$ higher than $R(T > 7.5\,\mathrm{K})$. The drop at $7.5\,\mathrm{K}$ is identified with the superconducting transition temperature $T_c$ of the junction. The superconducting transition of the Nb film was also measured via two contacts bonded to the Nb electrode of the actual device. We found $T_c = 8.5\,\mathrm{K}$ (inset of Fig. 5.3). A suppression of $T_c$ in a film from its bulk value of $9.5\,\mathrm{K}$ is commonly observed, as is a similar suppression of $T_c$ in micro-fabricated structures. The relative modest suppression of $\approx 1\,\mathrm{K}$ is in agreement with previous work, see for example Ref. [71].

The non-monotonic temperature dependence, which we observe in Fig. 5.3, suggests that the superconductor-2DEG interface has an intermediate transparency. This is qualitatively deduced by referring to the BTK model of a superconductor-normal metal junction.[52] In this model scattering is exclusively taking place at

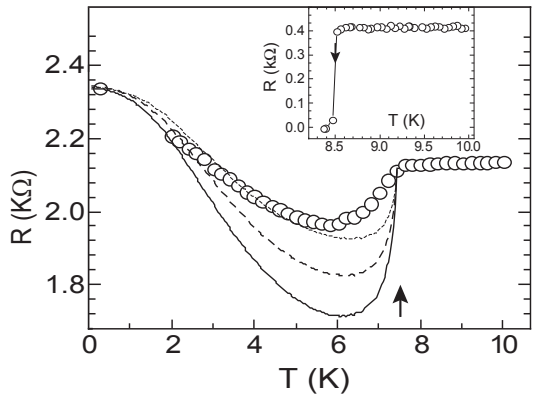


**Figure 5.3**: Temperature dependent resistance $R(T)$. Circles correspond to the measurements, whereas the curves are calculated using the BTK model together with a classical series resistor $R_S = 0$ (solid), $R_S = 500$ (dashed), and $R_S = 1000\,\Omega$ (dotted). $\Delta$ was fixed to 1.14 meV and the barrier transparency $\Gamma$ was fitted, yielding $\Gamma \approx 0.72$. The inset shows the superconducting transition of the Nb film measured with two probes on a structured device. The transitions of the Nb film and the sub-micron Nb contact are marked by arrows.

the junction interface described by a single parameter, which is the transmission probability (transparency) of the junction. This situation is referred to as the clean or ballistic junction limit (also the BTK limit), as opposed to the case in which additional scattering in the normal part of the junction is introduced. If the junction has a low transparency (tunnel junction), the resistance is expected to increase exponentially fast at low temperature. On the other hand, if the junction has a very high transparency, $R$ decreases monotonically to reach half of its normal state value at the lowest temperature. We neither see an exponential increase, nor a monotonic decrease of $R$, suggesting intermediate transparency.

In the following, if we refer to the normal state resistance $R_N$, we mean $R(\sim 8\,\mathrm{K})$, and if we refer to the resistance in the superconducting state $R_S$, we mean $R(270\,m\mathrm{K})$.

The measured normal-state resistance $R_N$ of this device equals $2.13\,\mathrm{k}\Omega$. It is straightforward to compare the corresponding normal-state conductance $G_N = R_N^{-1}$ with the Landauer formula,[94] i.e. with $G_N = (2e^2/h)N\Gamma$, where $N$ is the number of eigenchannels with non-zero transmission eigenvalues $\mathcal{T}_n$ and $\Gamma$ the mean value of $\mathcal{T}_n$. Taking $N$ to be 19, as determined from the width of the constrictions, yields $\Gamma \approx 0.32$ as the average transmission coefficient of the entire device. The resistance can have contributions from both the superconductor-2DEG interface and the point contacts to the normal reservoirs. Therefore, $\Gamma \approx 0.32$ must be seen as a lower bound for the S-N interface transparency. This will be studied in greater detail in section 5.4.

In Fig. 5.3 are also shown calculated curves of $R(T)$. The solid curve corresponds

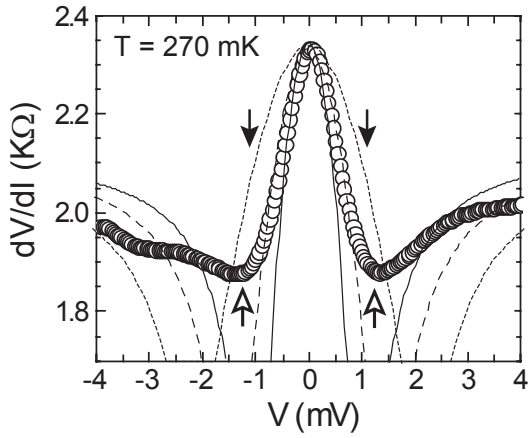


**Figure 5.4**: Voltage dependent differential resistance $dV/dI(V)$ measured at $T = 270\,\mathrm{mK}$. Circles correspond to the measurements, whereas the curves are calculated using the BTK model together with a classical series resistor $R_S = 0$ (solid), $R_S = 500$ (dashed), and $R_S = 1000\,\Omega$ (dotted). The parameters are similar to the ones used in Fig. 2. The full arrows point to the gap value $\Delta$ estimated from the transition temperature $T_c$ using the standard BCS relation $\Delta = 1.76 k_B T_c$, whereas the open arrows point to $\Delta = 1.9 k_B T_c$, where the factor 1.9 is known for bulk Nb.

to the BTK model for a junction transparency of 72 %. The minimum of $R(T)$ is much more pronounced in the calculated curve. In an attempt to account for additional scattering, for example at the constrictions of the beam-splitter, a classical series resistor was added (dashed and dotted curves). This clearly improves the overall matching, but strong deviations remain close to $T_c$.

We mention that similar resistance values and temperature dependencies were measured for several other samples.

We also measured the differential resistance $dV/dI$, which is shown as a function of voltage $V$ in Fig. 5.4. What actually was measured is $dV/dI$ as a function of bias current $I$. This data was converted to the displayed voltage dependence by integration. Similar to the temperature dependence, $dV/dI$ has a non-monotonic dependence. It first drops for increasing voltage and shows a minimum (a dip) before increasing again at higher voltages. The dip occurs close to the gap value $\Delta$ of the superconductor. $\Delta$ is estimated from the apparent transition temperature $T_c = 7.5\,\mathrm{K}$ of the junction using the zero-temperature BCS relation $\Delta = 1.76 k_B T_c$, yielding $\Delta = 1.14\,\mathrm{meV}$ (black arrows). The agreement is even better if we use instead of the BCS factor of 1.76 for the ratio $\Delta/k_B T_c$ the factor 1.9, which is the reported ratio for bulk Nb. This yields $\Delta = 1.23\,\mathrm{meV}$ (open arrows). Similar to $R(T)$, we used the BTK model to calculate the differential resistance, which is shown as a solid curve. The dashed and dotted curves correspond as before to the BTK model including a classical resistor in series. The theoretical curves display very pronounced

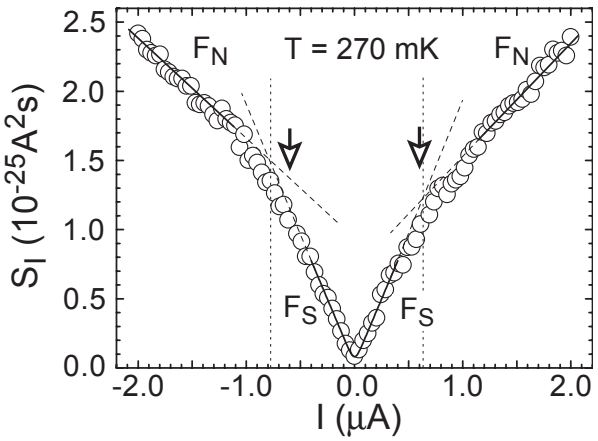


**Figure 5.5**: Power spectral density $S_I$ of the current noise of a sub-micrometer S-N junction as a function of applied current $I$. $S_I$ is extracted from the measured voltage noise $S_{V_1,V_2}$ between the superconductor and one of the normal reservoirs (see Fig. 1c) according to the Eq. 5.1. A clear crossover from a large Fano factor $F_S$ at small bias currents to a reduced Fano factor $F_N$ for large currents is observed. This crossover coincides with gap $\Delta$ of the superconductor (open arrows).

dips at $\pm\Delta$, which are apparently strongly damped in the measurements. Unlike in the temperature dependent case, i.e. $R(T)$, the series-resistor model improves the agreement only marginally. In particular the strong dips are not removed.

### 5.3.2 Shot-noise measurements

We measured the shot-noise from the superconductor to one of the normal reservoirs of the sub-micrometer beam-splitter as schematically shown in Fig. 5.1c. The measurement yields $S_{V_1V_2} = S_V$ as a function of bias current $I$. To obtain the intrinsic current noise $S_I(I)$ of the junction, Eq. 5.1 is applied using the calibration parameters as we have described it in the experimental part of Sec. 5.2. The result is shown in Fig. 5.5. It corresponds to the same sample, for which $R(T)$ and $dV/dI(V)$ have been shown in Fig. 5.3 and Fig. 5.4, respectively.

The full temperature and voltage dependence of the power-spectral density $S_I$ of the current fluctuations can only be expressed in a simple analytical form for a junction with a constant channel transmission coefficient $\mathcal{T}$. It is given by [22]

$$S_I = \frac{4(1-F)k_BT}{R} + F \cdot 2eIcoth\left(\frac{eV}{2k_BT}\right) \tag{5.2}$$

where $F$ is known as the Fano factor and equals $1-\mathcal{T}$.

Noise measurements are generally analyzed in two limiting cases: (a) for small applied voltages $eV << k_BT$, for which $S_I$ equals the Johnson-Nyquist equilibrium

noise (the thermal noise) $4k_BT/R$, and (b) for large applied voltages $eV >> k_BT$, for which a linear dependence of $S_I(I)$ is expected. In the limit of shot-noise, i.e. the latter case, $S_I = F \cdot 2eI$ and it is the Fano factor $F$, which is the central parameter that is deduced from such measurements.[48, 79, 1] $F = 1$ for a junction in which all channels have low transmission eigenvalues, i.e. in tunnel junctions.[48] In electronic devices in which charge is transported by single electrons alone, the Fano factor can in general be written as $F = \sum_n \mathcal{T}_n(1 - \mathcal{T}_n)/\sum \mathcal{T}_n$, which is always smaller or at most equal to one. Hence, the *suppression* of shot-noise in mesoscopic devices has been a central focus of research during recent years. For a review we refer to Ref. [1] and Ref. [83]. In contrast to 'normal' conducting devices, enhancement of shot-noise has recently been found in superconducting devices, in S-I-S [18] and S-N junctions,[19, 21] as well as in superconducting S-N-S links.[71, 87] The two extreme cases of S-N junctions are the tunnel junction and the ballistic junction. In the former, the noise in the superconducting state is doubled ($F_S = 2$) as compared to the normal state ($F_N = 1$).[18, 21] In the latter, shot-noise disappears completely, i.e. $F_S = F_N = 0$.

The doubling of the shot-noise in the superconducting state may be interpreted as being caused by the effective charge $e^\star$ of the charge carriers,[57, 51, 88, 84, 21] which are Cooper pairs with $e^\star = 2e$, provided the temperature and the applied voltage are sufficiently small. One has to emphasize, that the doubling of the shot-noise is not generic.[34] For a single channel S-N junction with transparency $\mathcal{T}$, the ratio of the Fano factors in the superconducting and normal state equals $F_S/F_N = 8/(2 - \mathcal{T})^2$, which - as mentioned before - can reach at most 2. If there are many channels with a distribution of eigenvalues $\mathcal{T}_n$, the situation is different. For example, there is a doubling from $F_N = 1/3$ to $F_S = 2/3$ in the diffusive case,[95, 19, 20] but $F_N = 1/4$ [15, 16] increases to $F_S = 0.604$ in case of an open chaotic cavity with a superconducting and normal terminal. The ratio in this case is even larger than 2, i.e. $F_S/F_N = 2.4$.

The measured shot-noise in Fig. 5 clearly displays two regimes in which $S_I(I)$ is nearly linear. In the low-current (low-voltage) regime, the slope is larger than in the high-current (high-voltage) regime. The crossover on the positive ($I > 0$) and negative ($I < 0$) side of the curve occurs at $\approx 0.62\,\mu A$ and $\approx -0.78\,\mu A$, corresponding to a voltage of $\approx 1.3\,\mathrm{mV}$ and $\approx -1.5\,\mathrm{mV}$, in reasonable agreement with the value of the superconducting gap parameter $\Delta/e = 1.23\,\mathrm{mV}$ (open arrows), which we have deduced before. The agreement is good on the positive side, but somewhat off on the negative side, where the crossover appears to be shifted to a larger value. Asymmetries in the crossover as well as in the Fano factors were seen in other samples too. The low and high-bias slopes are identified with $F_S$ (low-currents) and $F_N$ (high currents). We deduce $F_S = 0.58 \pm 0.10$ and $F_N = 0.25 \pm 0.04$ (average of slopes for $I < 0$ and $I > 0$). We note that the values of the Fano factors are considerably suppressed as compared to the case of a weakly transparent S-N junction.

In contrast to conductivity measurements, from which the average transmission

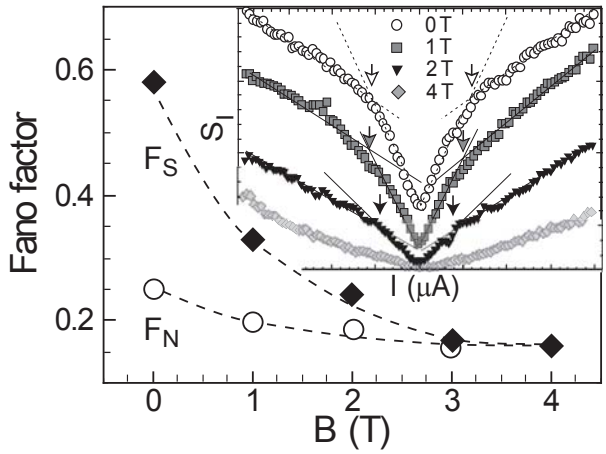


**Figure 5.6**: Fano factors versus perpendicular magnetic field $B$ (symbols). The dashed curves are guides to the eyes. As $B$ is increased, the enhancement of the Fano factor in the superconducting relative to the normal state (i.e. the ratio $F_S/F_N$) diminishes and fully disappears for $B \gtrsim 3\,\mathrm{T}$. Note, that $F_N$ also slightly decreases as the field increases. Inset: The power spectral density $S_I$ of the current noise as a function of the bias current $I$ for $B = 0$, 1, 2, and 4 T. The curves are shifted vertically for clarity. The crossover (arrows) between the superconducting and normal state shifts to lower voltages for increasing magnetic field as expected.

probability can be deduced, measurements of the shot-noise provide insight into the actual distribution of the transmission eigenvalues, which helps to find the correct description of the scattering problem of the actual device. By making use of all measured parameters, the resistance in the normal and superconducting state, as well as $F_S$ and $F_N$, different models will be compared in detail in the last section.

Finally, shot-noise measurements were also performed in a perpendicular magnetic field $B$, see Fig. 5.6. It is seen that the separation in two regimes, characterized by distinct Fano factors, disappears around $B = 3\,\mathrm{T}$, corresponding to the critical field of the Nb contact, which was measured independently. Fig. 5.6 also shows that not only the Fano factor $F_S$ in the superconducting state is suppressed, a decrease, though a smaller one, is also observed in the normal state for $F_N$. The origin is likely due to magnetic-field induced suppression of backscattering in the semiconductor nanostructure, a well known phenomenon in mesoscopic physics.[64] This observation proves that scattering is taking place within the beam-splitter in zero magnetic field adding up with the finite transparency of the superconductor-2DEG interface to the whole scattering problem. If we assume that ideally transmitting edge states have formed at the highest field, the superconductor-2DEG interface would have to account for the remaining Fano factor of $F_N = 0.16$ alone, yielding a transparency of as much as $\mathcal{T} = 1 - F_N = 0.84$ in a single channel model. From reference transport measurements on Hall-bars we know that the longitudinal resistance

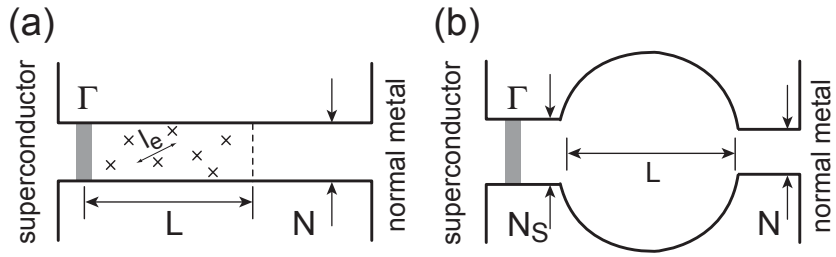


**Figure 5.7**: Illustration of the two basic models which we have used to analyze our data. (a) is based on a wire and (b) on a cavity. The models are considered in different regimes, but always in the limit of zero temperature. In (a) we distinguish between the ballistic ($l_e \gg L$), intermediate ($l_e \sim L$), and diffusive ($l_e \ll L$) regime, whereas in (b) the cavity is assumed to be either open on both sides (no barrier) or only open on one side with a tunnelling barrier on the other side, described by its transparency $\Gamma$.

of the 2DEG displays pronounced magnetic-field induced oscillations (Shubnikov-de Haas oscillations) for $B \lesssim 3\,\mathrm{T}$. Though the resistance minima do not yet reach zero, clear quantum Hall plateaus are discernible, see Fig. 5.1b. At 4 T, for example, the Hall measurements show that 10 Landau levels are occupied. Hence, the number of edge channels is already smaller than the number of transporting channels in zero magnetic field, which was estimated from the width of the constrictions to be 19. Since, transport follows the edges in the quantum Hall regime, the 84 % transmission at the S-N interface must be seen as an upper bound for the respective transmission probability in zero magnetic field.

In order to understand both the resistance and the shot-noise data, we need to thoroughly compare our data with a model consisting of a S-N contact with finite transparency to which an additional scattering region is added.

## 5.4 Discussion and Modelling

We compare the data of one device with a set of models. These models are schematically shown in Fig. 5.7. Fig. 5.7a is the wire model with a fixed number of channels $N$. Ideal contacts are assumed for the superconductor on the left and normal metal on the right side. The barrier, which may form in the processing of the Nb contact to the InAs 2DEG is captured by a tunnelling barrier with transparency $\Gamma$. A disordered region, parameterized by its length $L$ and elastic scattering mean-free path $l_e$, can be included. Fig. 5.7b is the cavity model. Here, both sides can have different numbers of channels. This is in fact closer to the real device geometry where the contact on the Nb side is wider than the constrictions at the Y-branch. The contact on the right is always assumed to be 'open', meaning that its conductance is equal to $NG_0$, where $G_0 = 2e^2/h$ is the quantum conductance, whereas there may be a tunnelling barrier in the left contact in order to model the effective transparency of

the N-S contact. In the following when we refer to 'the normal state' we consider the N-N case in which the superconductor is in the normal state. Similarly, when we refer to 'the superconducting state' we consider the S-N case. Note, that in contrast to the real device all the models have two terminals only. This simplification is likely to introduce deviations, because the open third terminal will add dephasing. However, neglecting dephasing (relaxation in general) facilitates the comparison with theory greatly. Now, we can use the machinery of mesoscopic physics to calculate the conductances and shot-noise Fano factors in the normal and superconducting state. It is one of the great hallmarks of mesoscopic physics that these quantities can be calculated in the coherent transport regime if the distribution $\rho(\mathcal{T})$ of transmission eigenvalues $\mathcal{T}$ for the particular device is known.

At zero temperature $T = 0$ the respective equations for the conductances $G_{(N,S)}$ and shot-noise powers $S_{(N,S)}$ in the normal ($N$) and superconducting ($S$) state are:[49]

$$G_N = G_0 N \int_0^1 d\mathcal{T}\,\rho(\mathcal{T})\mathcal{T} \tag{5.3}$$

$$G_S = G_0 N \int_0^1 d\mathcal{T}\,\rho(\mathcal{T})\frac{2\mathcal{T}^2}{(2-\mathcal{T})^2} \tag{5.4}$$

$$S_N = S_0 N \int_0^1 d\mathcal{T}\,\rho(\mathcal{T})\mathcal{T}(1-\mathcal{T}) \tag{5.5}$$

$$S_S = S_0 N \int_0^1 d\mathcal{T}\,\rho(\mathcal{T})\frac{16\mathcal{T}^2(1-\mathcal{T})}{(2-\mathcal{T})^4} \tag{5.6}$$

where $S_0 = 2eVG_0$ and $N$ is the total number of conducting channels in the system. Even more so, general concepts have been developed allowing to calculate the distribution function $\rho(\mathcal{T})$ for all models shown in Fig. 5.7.[96]

The result of this comparison is summarized in table 5.1. In the following we will go sequentially through the models and discuss the assumptions and results. We focus on the quantities $G_{(N,S)}$ and $F_{(N,S)}$ at zero temperature. In case of the simplest models we will also compare with the full temperature dependence of the conductance $G(T)$ and the voltage dependence of the differential conductance $dI/dV(V)$. The parameters $G_S$ and $G_N$ are deduced in the experiment from the linear-response conductance measured at the smallest temperature 270 mK and at $\sim 8$ K, respectively.

The simplest possible model to compare with is a S-N junction in which the normal part is ballistic. This problem was first considered by Blonder, Tinkham and Klapwijk and is known as the BTK model.[52] In the BTK model of a S-N interface, the junction is characterized by a single transmission coefficient, i.e. $\rho(\mathcal{T}) = \delta(\mathcal{T} - \Gamma)$. For $\Gamma = 1$, the junction resistance decreases with decreasing temperature and the conductance is doubled at $T = 0$ K due to Andreev reflection. In the opposite limit $\Gamma \ll 1$, Andreev reflection is suppressed and the resistance

increases monotonically with decreasing temperature below $T_c$. The comparison of the equations for $G_N$ and $G_S$ with the experimental values yields $\Gamma = 0.73$ and $N \approx 9$. We can now use these two parameters to calculate the full temperature and the non-linear voltage dependence of the conductance and compare both with the measurements. This is shown in Fig. 5.3 and 5.4 where the calculated curves are the solid ones. Fig. 5.3 shows the temperature dependence of the linear two-terminal resistance $R(T)$ and Fig. 5.4 the differential resistance $dV/dI$ as a function of voltage $V$, measured at $T = 270\,\mathrm{mK}$. As imposed by this procedure the measured (circles) and calculated (solid) curves in Fig. 5.3 match at zero temperature and at (or above) $T_c$ in the normal state. Similarly, the measured (circles) and calculated (dashed) curves in Fig. 5.4 match at zero bias and approximately at the largest bias voltage of $|V| = 4\,\mathrm{mV}$ at which one closely approaches the normal state. In the intermediate temperature and voltage regime substantial deviations are found. The theory predicts a much larger conductance increase in the intermediate regime than is seen in the experiment. This is particularly striking in the differential resistance where a strong dip (or a peak in the conductance) is expected to occur near the superconducting gap $\Delta$.

The experimentally observed strong damping of this conductance peak near the superconducting gap has also been seen in other work.[91, 97] It can be caused by pair-breaking due to inelastic scattering. Even more so, the shape of the quasi-particle density-of-state in the vicinity of $\pm\Delta$, which acquires singularities in the BCS model, may strongly be damped at the interface between the Nb and the 2DEG.[91] The reason for the latter may be a disordered interface caused by sputter cleaning or by partial oxidation. For the former, we suspect that the second terminal of the Y-branch, which has been left open, is a source of dephasing. Electrons at the Y-branch can scatter into the drain contact, but may also be scattered into the third terminal, from which they are reflected back but with unknown phase. In addition, the large deviations in the intermediate regime may also stem from the assumed model, which is likely to be too simple. We will come back to this issue when we refine the model. Let us now see wether the ballistic BTK model can capture the shot-noise results, i.e. the measured Fano factors. In case of an N-N barrier, the Fano factor is given by $F_N = 1 - \Gamma$. The estimated $\Gamma = 0.73$ predicts $F_N = 0.27$, which is consistent with the measured shot-noise Fano factor of 0.25. In the superconducting state, however, the theory for a S-N barrier [49] predicts $F_S = 8(1-\Gamma)/(2-\Gamma)^2 = 1.34$, whereas the measured Fano factor is substantially smaller and amounts to 0.58 only. We may also do the reverse and deduce the transparency $\Gamma$ from the measured Fano factors instead. $F_S = 0.58$ then implies $\Gamma = 0.91$ which is both inconsistent with the measured Fano factor in the normal state $F_N$ and with the temperature dependence of the resistance in Fig. 5.3. Hence, the ballistic junction model does not yield consistent values. This is not surprising, because of the structured beam-splitter in front of the superconductor. Each arm of the splitter is comprised of a relatively narrow opening. Hence, parts of the

**Table 5.1**: Comparison of the measured data, i.e. the linear conductance $G_{(N,S)}$ and the shot-noise Fano factors $F_{(N,S)}$ in the normal ($N$) and superconducting ($S$) state with various models. Schematics for the models are shown in Fig. 5.7a and b.

| | | $G_N/G_0$ | $G_S/G_0$ | $F_N$ | $F_S$ | $\Gamma$ | $N$ |
|---|---|---|---|---|---|---|---|
| Measured | | 6.1 | 5.5 | 0.25 | 0.58 | | |
| L $\ll l_e$ | Ballistic | 6.1 | 5.5 | 0.27 | 1.34 | 0.73 | 9 |
| | Ballistic + $R_S$ | 6.1 | 5.5 | 0.16 | 0.80 | 0.72 | 11 |
| L $\gg l_e$ | Diffusive | 5.8 | 5.8 | 0.33 | 0.67 | 1 | 19 |
| L $\sim l_e$ | Open Cavity | 5.4 | 6.4 | 0.25 | 0.60 | 1 | 11 |
| | Quasi-ballistic | 6.1 | 5.5 | 0.36 | 0.77 | 0.55 | 17 |
| | Cavity + barrier | 6.1 | 5.6 | 0.33 | 0.84 | 0.7 | 11 |

eigenchannels emanating from the Nb-2DEG interface must be back reflected at these exit ports. This results in an additional voltage drop, i.e. in an additional resistance. Since the sample is likely to be coherent this resistance cannot simply be treated as a classical series resistor. The whole structure composed of S-N interface, cavity and exit leads need to be treated as one scattering problem. We will discuss this latter on, but still try the classical series resistor model as an additional test case next.

Fits to the measured two-terminal resistance $R(T)$ and $dV/dI(V)$ including a classical resistor $R_S$ in series to the S-N interface are shown in Fig. 5.3 and Fig. 5.4 for two values of $R_S$, i.e. $R_S = 500$ and $R_S = 1000\,\Omega$. It turns out that if $R_S$ is increased, the fit of $R(T)$ improves in the intermediate temperature regime. However, the width of the zero-bias peak in $dV/dI$ broadens with increasing $R_S$, so that the agreement gets worse here. A reasonable compromise is found for $R_S = 500\,\Omega$. Using the conductance measurements we deduce a junction transparency of $\Gamma = 0.72$ and obtain for the number of channels $N \approx 11$ within this model. Because the series resistor is a classical one it does not contribute to non-equilibrium shot-noise. In order to deduce the Fano factor the current fluctuations $S_I$ have to be plotted versus current $I$. $S_I$ is obtained from the measured voltage fluctuations by dividing $S_V$ with the total resistance $R = R_{SN} + R_S$ squared. In the framework of this model this division is incorrect. Instead, one should divide by $R_{SN}^2$, only. This now yields a correction factor amounting to $(1 + R_S/R_{SN})^2$, which has to be applied to the measured data. For ease of comparison, we apply the inverse $1/(1+R_S/R_{SN})^2 \approx 0.60$ to the model calculation. As a result, the predicted Fano factor in the superconducting state $F_S = 0.80$ is getting closer to the measured value, but $F_N = 0.16$ is now clearly too small as compared with the measured value. Adding a classical series resistance improves somewhat the agreement between the experiment and model of $R(T)$. It also relaxes slightly the large discrepancy of the Fano factor in the superconducting state. However, it is clear that this model is an oversimplification, because the de-

vice is more than just one junction with a single transparency and the whole device, including the cavity and beam-splitter should be treated on equal footing.

A fixed transparency is a very idealized assumption, one which never holds true in a practical multi-channel device. There are many reasons why a distribution of transparencies has to be considered: the junction interface is never perfectly homogeneous, the sample has been structured and the boundaries may be rough on the scale of the Fermi wavelength and there are dopants within the heterostructure. It is possible that the quality of the 2DEG was degraded near the S-N interface during the sample processing, for example, due to the Ar sputtering of the MESA prior to Nb deposition.[91] In addition, the narrow constrictions defining the output ports must be seen as a scattering center. If we assume that disorder is substantial, we are led to the diffusive regime, which is another limiting case contrasting with the ballistic junction limit discussed before. For a diffusive conductor, the distribution of transmission eigenvalues $\rho(\mathcal{T})$ is given by a universal result $1/(2s\mathcal{T}\sqrt{1-\mathcal{T}})$, where $s = L/l_e$.[9] Using this distribution function yields $G_S/G_N = 1$,[56] $F_N = 1/3$,[9] and $F_S = 2/3$.[51] As can be seen from the table, the agreement is much better, in particular for the Fano factors, suggesting that elastic scattering must be considered. However, the measured conductances are not equal in the normal and superconducting state, i.e. $G_S/G_N = 1$, as predicated by this model. Though the agreement is much better, this model is an oversimplification too. We know that the scattering-mean-free path in the bulk of the 2DEG is much larger than the size of the nanostructure which is considered here. In addition, the magnetic-field dependence of the Fano factor $F_N$ in the normal state (Fig. 5.6) is inconsistent with a diffusive conductor. One should therefore rather view the device as a cavity with three terminals: a wide Nb one, and two narrow leads defined by the constriction. This justifies to compare our data also to an open chaotic cavity.

We only compare our data in table 5.1 with the symmetric cavity, because this is suggested by the measured Fano factor in the normal state, which is found to be close to $F_N = 0.25$. A suppression factor of 1/4 is the expected result for the symmetric open cavity.[15, 83, 16] The distribution of transmission eigenvalues $\rho(\mathcal{T})$ for a chaotic cavity, contacted by two open leads each having $N$ ideally transmitting channels, is given by another bimodal distribution function $1/\pi\sqrt{\mathcal{T}(1-\mathcal{T})}$.[15, 49] Using Eq. 5.3-5.6 yields: $G_N/G_0 = N/2$, $G_S/G_0 = (2-\sqrt{2})N$, $F_N = 0.25$, and $F_S = 0.6036$. As can be seen from table 5.1, the measured Fano factors compare very well with this model. On the other hand, this model predicts $G_S > G_N$, whereas $G_S < G_N$ in the experiment. We mention that $G_S > G_N$ also holds if the cavity is allowed to be asymmetric. In fact, $G_S/G_N$ is minimal for the symmetric cavity and reaches the well known factor of two for strong asymmetries. This shows that we cannot cure the deficiency in the conductances between theory and model just by tuning the asymmetry alone. In an attempt to lower $G_S$ as compared to $G_N$ we now further try to refine our model. There are two refinements we can consider: We may start from the 'universial' diffusive case and ask the question what happens if

the elastic scattering mean-free path $l_e$ is increased up to the point when $l_e$ becomes of the order of the device size (i.e. cavity size). Secondly, we may add additional scattering by adding a barrier to one side of the open cavity.

We first consider the 'quasi-ballistic' case studied by De Jong and Beenakker. [51, 49] In their model of a S-N device, a tunnel barrier is inserted (which may be used to model the quality of the contact itself) in series to a disordered region of length $L$ in which the elastic scattering length is $l_e$. De Jong and Beenakker were able to study the crossover from the ballistic to the diffusive regime for an arbitrary ratio of $s = L/l_e$. We have already considered the limiting cases $s = 0$, which is the ballistic BTK limit, and the universal diffusive case $s \to \infty$. Interesting for us is the intermediate case $s \sim 1$, which can be computed for both the normal and the superconducting state using the scaling theory of the generalized conductance.[51, 95] The numerical calculation yields $\Gamma = 0.55$ and $N = 17$ for $s \sim 1$. De Jong and Beenakker also showed that the shot-noise power can vary between zero and twice the Poisson value, depending on the junction parameters.[51] Using $\Gamma = 0.55$ and $N = 17$, we obtain for the Fano factors $F_N = 0.36$ and $F_S = 0.77$.

In view of the real device geometry, a refinement of the open cavity model is appealing too. The real device is asymmetric in that the width of the contact at the Nb side is wider than the constrictions at the exits. In addition, there is likely a barrier at the interface of the 2DEG and the superconductor, the transparency of which has been denoted by $\Gamma$ in the previous models. The simplest way to calculate $\rho(\mathcal{T})$ is to apply circuit theory [96] to the series connection of a tunnel junction with a quantum-point contact (QPC). The tunnel junction is the element at the Nb side. It is parameterized by its conductance $G_t$. The QPC models the narrow constriction on the right side. It is parameterized by its conductance $G = (2e^2/h)N$, i.e. by the number of (open) channels. Though $\Gamma$ does not appear in the model explicitly (only the ratio $G/G_t$ enters), it can be extracted from the fitted value which we obtain for $G_t$. $G_t$ can be expressed as $G_0 \Gamma N w_S/w_N$, where $w_{S,N}$ is the width of the 2DEG at the S and at the N side, respectively. In trying to find the best match, we fix the conductance in the normal state to the measured value and vary $N$ to get the best agreement with all measured parameters. This approach yields $N = 11$, $\Gamma = 0.7$, $F_N = 0.33$, and $F_S = 0.84$.

Let us summarize the results of all the models. One may say that none yields perfect agreement in all four measured parameters, i.e. $G_N$, $G_S$, $F_N$, and $F_S$. The most realistic ones in terms of the actual geometry, i.e. the quasi-ballistic and cavity with barrier models, yield reasonable agreement in all parameters. The Fano factors are predicted to be slightly larger than measured. In fact, this trend holds true for all models considered. The measured Fano factors are systematically smaller. We suspect that the origin for this discrepancy is found in the third terminal, i.e. the second outgoing lead of the Y-branch, which was left open in the measurements of the conductance and noise. Electrons entering into this lead will relax and thermalize before being re-injected into the device again. Relaxation in general reduces shot-

noise.[98, 99, 100, 22, 101] With regard to the number of channels the different models predict $N = 9 \ldots 17$ for the channel number in the constriction. This is in fair agreement with an estimate of the channel number based on the lithographic width and the Fermi wavelength, yielding $N \sim 19$. It is quite reasonable that the channel number deduced electrically turns out to be somewhat smaller, because of depletion in the vicinity of the MESA after etching.

## 5.5 Outlook and conclusions

In summary, we have realized a mesoscopic superconductor-normal beam-splitter geometry in a solid state hybrid system. We can account for both the conductance and shot-noise data by modeling the device as a highly transparent S-N interface connected in series with a 'short' scattering region, which is in the quasi-ballistic transport regime. The scattering region is formed by the cavity in the 2DEG between the S-N interface and the two constrictions forming the electron beam-splitter. The shot-noise measured across the superconductor and one arm of the beam-splitter is enhanced relative to the normal state. The respective Fano factors are in reasonable agreement with the Landauer description (scattering problem) of coherent transport. Residual deviations, in particular in the vicinity of the gap energy in the differential conductance measurements, are likely due to relaxation, a source of which is the second arm of the beam-splitter which was left open in the reported experiments. Current fluctuations can be suppressed by an extra terminal, even in the absence of a net (average) current.

Our devices are very well suited to explore positive cross-correlations,[59] as have recently been predicted in several theoretical papers.[59, 61, 35, 27, 62, 40] Of these theoretical treatments, Ref. [40] is in closest correspondence with our experiments. In Ref. [40], an electron cavity is connected to one superconducting and two normal leads via point contacts. Positive correlations are predicted to appear for a dominant coupling to the superconducting lead. The devices which we have studied in this work have roughly similar couplings to the S and N leads. In the next step, one has to make use of the ability of semiconductors to tune the transparency of the constrictions with additional electrodes (split gates), which can be fabricated self-aligned with the etched trenches. This would greatly help in the search for positive correlations in solid-state nanostructures.

## Appendix A

# *Calculation of the transfer function*

We need to know following elements in order to extract the spectrum of current fluctuations $S_I$ from measured voltage fluctuations $S_{V_1,V_2}$:

1. The Bias resistance $R_B$ : The measured value of $R_B$ at low temperature was $\sim 1.037$ M$\Omega$.

2. The spectral density of the bias resistance $R_B$ : The bias resistance is thermally anchored at the bottom of 1K pot in $^3$He system so that the temperature of the resistance is about to that of 1K pot which has the actual measured temperature of $\sim$ 1.9K. Thus the equilibrium (Thermal) noise of the bias resistance is $S_B = 4k_BT/R_B \sim 1.0 \times 10^{-28}\mathrm{A}^2/\mathrm{Hz}$ where, $k_B$ is the Boltzmann constance and $R_B$ is the resistance of bias resistor.

3. The total capacitance $C_{tot}$ of the setup: In our consideration, the main contribution to the total capacitance is the capacitance from the bias lines $C_B$ and the pair of noise detecting leads together with the amplifiers $C_L$. i.e. $C_{tot} = C_B + 2C_L$. From the independent measurement, we get $C_B = 230$ pF and $C_L = 335$ pF respectively. Alternatively, one can determine the total capacitance of the measurement setup from the fits of the frequency dependence of the measured voltage fluctuation spectrum $S_{V_1,V_2}$ for various sample resistances and frequencies (See Fig.4.4b). We found a reasonable agreement with the measured value of 900 pF.

4. The noise measurement line resistance $R_L$ : The SMA cable was used for the measurement lines of noise and it does not have any extra filters at room temperature. $R_L \approx 30\Omega$.

5. The spectral density of the current noise source of the amplifier: The input current noise of the preamplifier is determined by measuring the output voltage fluctuations when the high resistance is connected at the input of the preamplifier. The preamplifier input stage is characterized by its gain $G$, input resistance $R_{in}$ and input capacitance $C_{in}$ and its current and voltage noise sources $i_n$ and $v_n$ (See Fig.A.1).

First, let us characterize one of the pre-amplifier with a model circuit shown in Fig.A.1. We use very simple and powerful method, "superposition principle" : Calculate one element by one element simply by putting others 'short' for the voltage sources and 'open' for the current source when they are not in calculation. We see from Fig.A.1 that there are three possible sources for the noise $V_S$, $v_n$ and $i_n$ which are the external voltage source, voltage noise source and current noise source of the amplifier respectively. From the first voltage source $V_S$, we get the output voltage:

$$V_{out,1} = G\frac{R_{in}V_S}{R_{in} + R_S + j\omega C_{in}R_{in}R_S}\,. \tag{A.1}$$

Secondly, the voltage noise source $v_n$ in the amplifier itself contribute to the output voltage directly, i.e. $V_{out,2} = Gv_n$ and finally, the current noise source in amplifier $i_n$ made the noise contribution of:

$$V_{out,3} = G\frac{(R_{in}R_S)i_n}{R_{in} + R_S + j\omega C_{in}R_{in}R_S}\,. \tag{A.2}$$

Thus, the total output voltage from the amplifier is,

$$\begin{aligned} V_{out} &= V_{out,1} + V_{out,2} + V_{out,3} \\ &= G\Big\{v_n + \frac{R_\parallel}{1 + j\omega C_{in}R_\parallel}\Big(\frac{V_S}{R_S} + i_n\Big)\Big\}\,. \end{aligned}$$

where $R_\parallel = R_{in}R_S/(R_{in} + R_S)$. In equilibrium, $V_S$ is just Johnson-Nyquist voltage noise source of $R_S$ and the output spectral density $S_{out}$ is given by

$$S_{out} = G^2\Big\{S_V + \frac{R_\parallel^2}{1 + (\omega C_{in}R_\parallel)^2}\Big(\frac{4k_BT}{R_S} + S_{Amp}\Big)\Big\}\,. \tag{A.3}$$

where $S_V$ is the spectral density of $v_n$ and it can be measured by the shorting the input of the amplifiers, i.e., $S_{out} = G^2S_V$. Here we measured $S_V$ of the two NF-LI75 amplifiers. Measured noise of two preamplifier was almost identical. See Fig. A.2.

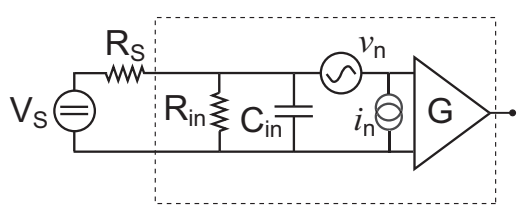


**Figure A.1**: Model of the amplifier with some resistance $R_S$ and DC voltage source $V_S$ at the input of the amplifier.

It consists of a white noise part and a $1/f$ component and from the fit, we get the reasonable value of spectral density

$$S_V(f) = 2.4 \times 10^{-18} + \frac{1.05 \times 10^{-15}}{f} [V^2/Hz] \,. \tag{A.4}$$

For checking the current noise power spectrum from the amplifiers, we have to measure first, the transfer function $R_{\|}^2/1+(\omega C_{in} R_{\|})^2$ using a broad-band AC source in series with $R_S$. In the next step, the spectral density $S_{out}$ is measured by the spectrum analyzer HP 89410A with the source resistance $R_S$ connected to the input of the amplifier. Different resistances (10kΩ, 100kΩ, 1MΩ) were used and last two give the same values of $S_{Amp} \sim 5 \times 10^{-28} A^2/Hz$. Fig. A.2 shows both voltage and current spectral density of the NF-preamplifier.

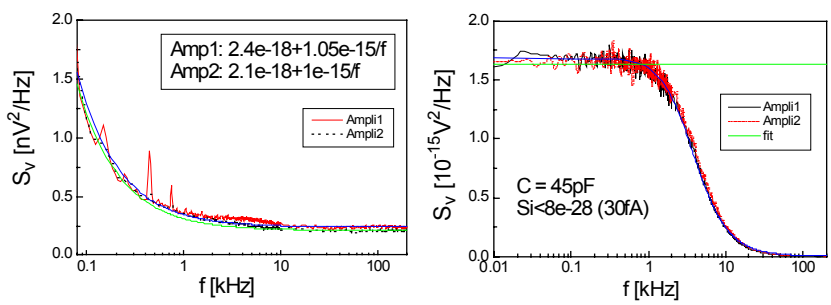


**Figure A.2**: (a)The spectral density of the voltage noise $v_n$ of NF-LI75 preamplifier. It can be measured by the shorting the input of the amplifiers, i.e. $S_{out} = G^2 S_V$. Here we measured $S_V$ of the two NF-LI75 amplifiers. It constitute with a white noise part and $1/f$ component. (b) The spectral density of the current noise of the amplifier. From this we deduce the capacitance of the amplifier 45 pF for each.

We would like to turn to the characterization of the noise measurement setup using the model circuit depicted in Fig.4.5. once again. However, at this time, we calculate the expression of $V_1$ and $V_2$ including the capacitance of the voltage lines $C_L$ and keep all the terms in the expression. The expression is getting more complicated than the previous one and yields for $V_1$, $V_2$ :

$$V_1 = v_1 + \frac{R_S(i_B + i + i_1 + i_2) + \left[R_L\left(\frac{R_S}{R_B} + 1 + j\omega R_S C\right) + \frac{j\omega R_L R_S C_L}{1+j\omega R_L C_L}\right] i_1}{(1 + j\omega R_L C_L)\left(\frac{R_S}{R_B} + 1 + j\omega R_S C\right) + 2j\omega R_S C_L}$$

$$V_2 = v_2 + \frac{R_S(i_B + i + i_1 + i_2) + \left[R_L\left(\frac{R_S}{R_B} + 1 + j\omega R_S C\right) + \frac{j\omega R_L R_S C_L}{1+j\omega R_L C_L}\right] i_2}{(1 + j\omega R_L C_L)\left(\frac{R_S}{R_B} + 1 + j\omega R_S C\right) + 2j\omega R_S C_L}$$

. The cross-correlation of the two output voltages $\langle \overline{V_1} \cdot V_2 \rangle$ is given by:

$$\begin{aligned} S_{V_1,V_2} &= \langle \overline{V_1} \cdot V_2 \rangle \\ &= \overline{Z_1} \cdot Z_1 \Big( \langle \overline{i_B} \cdot i_B \rangle + \langle \bar{i} \cdot i \rangle \Big) + \overline{Z_2} \cdot Z_1 \langle \overline{i_1} \cdot i_1 \rangle + \overline{Z_1} \cdot Z_2 \langle \overline{i_1} \cdot i_1 \rangle \\ &= \overline{Z_1} \cdot Z_1 (S_B + S_I) + (\overline{Z_1} \cdot Z_2 + \overline{Z_2} \cdot Z_1) S_{amp}\,, \end{aligned} \tag{A.5}$$

where

$$Z_1 = \frac{R_S}{(1 + j\omega R_L C_L)\left[1 + j\omega R_S C_B + \frac{R_S}{R_B}\right] + 2j\omega R_S C_L} \tag{A.6}$$

$$Z_2 = \frac{R_S + R_L\left[1 + j\omega R_S C_B + \frac{R_S}{R_B}\right] + \frac{j\omega R_S R_L C_L}{1+j\omega R_L C_L}}{(1 + j\omega R_L C_L)\left[1 + j\omega R_S C_B + \frac{R_S}{R_B}\right] + 2j\omega R_S C_L}\,. \tag{A.7}$$

We also calculate the power spectrum of the current fluctuations of the sample $S_I$ from the measured cross-correlation spectrum $S_{V_1,V_2}$ in the same way as before

$$S_I = \frac{1}{|Z_1|^2} \cdot S_{V_1,V_2} - S_B - 2\frac{Re\{\overline{Z_1} Z_2\}}{|Z_1|^2} \cdot S_{amp}\,. \tag{A.8}$$

where $Re\{Z\}$ is the real part of the complex number $Z$ and

$$\begin{aligned} \frac{1}{|Z_1|^2} &= \frac{1}{R_S^2}\left(1 + \frac{R_S}{R_B} - \omega^2 R_L R_S C_L C_B\right)^2 \\ &+ \frac{\omega^2}{R_S^2}\left(R_S C_B + R_L C_L \frac{R_S}{R_B} + R_L C_L + 2R_S C_L\right)^2 \end{aligned} \tag{A.9}$$

and

$$\frac{Re\{\overline{Z_1} Z_2\}}{|Z_1|^2} = 1 + \frac{R_L}{R_B} + \frac{R_L}{R_S} + \frac{\omega^2 R_L^2 C_L^2}{1 + \omega^2 R_L^2 C_L^2}\,. \tag{A.10}$$

Recalling the previous conditions, $\omega R_L C_L \ll 1$, $R_L/R_B \ll 1$ and $R_L/R_S \ll 1$, the right-hand side of the Eq.A.9 and A.10 are simplified to

$$\frac{1}{|Z_1|^2} = \frac{1 + (wC_{tot}R_{\|})^2}{R_{\|}^2} \qquad , \qquad \frac{Re\{\overline{Z_1}Z_2\}}{|Z_1|^2} = 1 + \frac{R_L}{R_{\|}} \,,$$

where $R_{\|} = R_B R/(R_B + R)$ and $C_{tot} = C_B + 2C_L$. Hence, finally the power spectrum of the current fluctuations of the sample $S_I$ is found to be

$$S_I = \frac{1 + (\omega C_{tot}R_{\|})^2}{R_{\|}^2} S_{V_1,V_2} - S_B - 2\Big(1 + \frac{R_L}{R_{\|}}\Big) S_{Amp} \,. \tag{A.11}$$

## Appendix B

# *Process recipes*

### Ohmic contact[1]

- Rinse the InAs substrate with acetone and ethanol and blow dry with $N_2$ gun.
- Spin PMMA at 6000rpm for 40 sec.(Time is set in the spinner).
- Bake at 175°C for 30 min in the oven.
- Expose using I = 16 nA (Acceleration voltage = 35kV, Dose = 480 $\mu$C/cm$^2$).
- Develop PMMA in MiBk : IPA = 1 : 3 for 45 sec.
- Rinse in IPA and blow dry with $N_2$ gun.
- Clean the surface by RIE(Oxygen plasma) ($O_2$ = 22%, Base pressure = 2e-5 mbar, Process pressure $\sim$ 250 mTorr, DC voltage = 110 $\sim$ 125 V, RF-Forward $\sim$ 50 W, RF-backward $\sim$ 5 W, time = 60 sec ).
- Dip in Hcl (37%) for 5 sec. to remove oxide layer.
- Evaporate the multilayers of (Ni 6 nm/Au 50 nm/Ge 20 nm/Au 60 nm/Ni 30 $\sim$ 40 nm)
- Lift off in Acetone
- Anneal the multilayer (120°C for 600 sec. in type 3, Pressure = 310 mbar $\rightarrow$ 275°C for 120 sec. in type 3, Pressure 320 mbar).
- Check the contact resistance with probe station. It should shows few hundred ohms or less.

[1]The alignment marks are formed at the same time with the ohmic contacts

### MESA etch

- Spin PMMA at 6000rpm for 40 sec.
- Expose of MESA etch structure (Beam current = 16 nA, Acceleration voltage = 35kV, Dose = 480 $\mu$C/cm$^2$).
- Develop PMMA in MiBk : IPA = 1 : 3 for 45s.
- Wet-etch of heterostructure with $H_3PO_4$ : $H_2O_2$ : $H_2O$ = 1 : 1 : 100 for 90s (Typical etchant temperature $\sim$ 28°C).
- Stop etch with DI-water and blow dry with $N_2$ gun.
- Inspect with the optical microscope.

### Nb deposition with PMGI resist

- Spin PMGI resist (PMGI 11 % in CP/THFA[2] : Cyclopentanone = 7:1) at 4000rpm for 40 sec.
- Soft bake on hotplate at 250°C for 2 min. ( $\rightarrow$ thickness $\sim$ 600nm)
- Evaporate Ge of thickness $\approx$ 50 nm.
- Spin PMMA at 6000rpm for 40 sec. and bake in oven for 30 min ($\rightarrow$ thickness of 630 nm).
- Expose (Beam current = 16 nA, Acceleration voltage = 35kV, Dose = 480 $\mu$C/cm$^2$).
- Develop the PMMA in MiBk : IPA = 1 : 3 for 45s.
- RIE of Ge with $CHF_3$ : $O_2$ = 34 : 4 for 5 min. (etch rate $\sim$ 29nm/min.)
- RIE of PMGI with $O_2$ plasma for 3 min. ($O_2$ = 16%, Process pressure $\sim$ 250 mTorr, RF-Forward = 100 W $\rightarrow$ etch rate $\sim$ 250 nm/min.)
- Evaporation of Nb of thickness $\sim$ 100 nm.
- Lift off with warm (50°C) MR 1165 remover for at least 30 min.

[2]Information in technical data sheet of NANO™ PMGI SF 11 from MicroChem Corp.

### Nb deposition procedure from NTT

- Clean the substrate at 160°C for 10 min. in Ozone gas.
- Spin Poly (Phenyl Methacrylate-Co-Methacrylic Acid) resist[102, 103] at 6000 rpm for 50 sec. → Resist thickness : 300 ∼ 500 nm.
- Pre-bake in Oven at 200°C for 50 min.
- Expose in JEOL JBX-6000FS (Acceleration voltage = 50 kV, Beam current = 100 pA, Dose = 80 ∼ 160 $\mu$C/cm$^2$)
- Develop in MIBK : ECH[3] = 2 : 1 for 60 sec.
- Rinse in ECH for 60 sec.
- Post-bake in Oven at 115°C for 10min.
- Etch the heterostructures with Citric acid (20%): $H_2O_2$ = 20 : 1 for 60 sec. → etching depth ∼ 60 nm.
- RF sputter cleaning with the power 10 W for 5 min in Ar gas at the pressure 5 mTorr.
- Deposit Nb of thickness ∼ 80 nm ( Background pressure before deposition is $< 10^{-9}$ Torr, Deposition rate ∼ 0.5 nm/sec.)[4]
- Lift-off in Acetone for 1 hour with ultrasonic vibration.

### Mesoscopic beam splitter

- Spin PMMA at 6000rpm for 40 sec.
- Bake at 175°C for 30 min in the oven.
- Exposure (For fine structures, Beam current = 40 pA, Acceleration voltage = 35kV, Area step size = 4.6 nm, Area dwell time = 4.2 $\mu$s., Area Dose ∼ 400 $\mu$C/cm$^2$, Line step size = 4 nm, Line dwell time = 40 ∼ 70 $\mu$s., Line Dose = 300 ∼ 480 $\mu$C/cm$^2$).
- Develop PMMA in MiBk : IPA = 1 : 3 for 45 sec.
- Rinse in IPA and blow dry with $N_2$ gun.

[3] Ethylcyclohexane

[4] Nb electrodes were angle-deposited by electron beam deposition, where the sample was tilted at 30 degree to the horizontal line

- Fine wet etch with $H_3PO_4 : H_2O_2 : H_2O = 1 : 1 : 100$ for 60s.
- Stop etch with DI-water and blow dry with $N_2$ gun.
- Inspect with Philips SEM.

### Gate-test sample

- Clean the substrate with acetone and ethanol
- Spin PMMA at 6000rpm for 40 sec.
- Bake at 175°C for 30 min in the oven → thickness of ∼ 630 nm.
- A mesa definition by wet-etching (Refer the section MESA etch, etch depth ∼ 150 nm).
- Alloyed Au-Ge-Ni ohmic contacts to the 2DEG (Refer the section Ohmic contact).
- The fine structures etch (Refer the section Mesoscopic beam splitter, etch depth ∼ 150 nm)
- Gate definition by evapotation of 4 nm Ti and 100 nm Au.

# *Bibliography*


[1] C. Beenakker and C. Schönenberger, Phys. Today **may 2003**, 37 (2003).

[2] W. Schottky, Ann. Phys. (Leipzig) **57**, 541 (1918).

[3] L. Saminadayar, D. C. Glattli, Y. Jin, and B. Etienne, Phys. Rev. Lett. **79**, 2526 (1997).

[4] R. de Picciotto97, M. Reznikov, M. Heiblum, V. Umansky, G. Bunin, and D. Mahalu, Nature **389**, 162 (1997).

[5] M. Reznikov, R. de Picciotto, T. G. Griffiths, M. Heiblum, and V. Umansky, Nature **399**, 238 (1999).

[6] R. Cron, M. F. Goffmann, D. Esteve, and C. Urbina, Phys. Rev. Lett. **86**, 4104 (2001).

[7] Y. P. Li, A. Zaslavsky, D. C. Tsui, M. Santos, and M. Shayegan, Phys. Rev. B **41**, 8388 (1990).

[8] H. C. Liu, J. Li, G. C. Aers, C. R. Leavens, M. Buchanan, and Z. R. Wasilewski, Phys. Rev. B **51**, 5116 (1995).

[9] C. W. J. Beenakker and M. Büttiker, Phys. Rev. B **46**, 1889 (1992).

[10] K. Nagaev, Phys. Lett. A **169**, 103 (1992).

[11] F. Liefrink, J. I. Dijkhuis, M. J. M. de Jong, L. W. Molenkamp, and H. van Houten, Phys. Rev. B **49**, 14066 (1994).

[12] A. H. Steinbach, J. M. Martinis, and M. H. Devoret, Phys. Rev. Lett. **76**, 3806 (1996).

[13] R. J. Schoelkopf, A. A. K. P. J. Burke, D. E. Prober, and M. J. Rooks, Phys. Rev. Lett. **78**, 3370 (1997).

[14] M. Henny, S. Oberholzer, C. Strunk, and C. Schönenberger, Phys. Rev. B **59**, 2871 (1999).

[15] R. A. Jalabert, J. L. Pichard, and C. W. J. Beenakker, Europhys. Lett. **27**, 255 (1994).

[16] S. Oberholzer, E. Sukhorukov, C. Strunk, C. Schönenberger, T. Heinzel, and M. Holland, Phys. Rev. Lett. **86**, 2114 (2001).

[17] S. Oberholzer, E. Sukhorukov, and C. Schönenberger, Nature **415**, 765 (2002).

[18] P. Dieleman, H. G. Bukkems, T. M. Klapwijk, M. Schicke, and K. H. Gundlach, Phys. Rev. Lett. **79**, 3486 (1997).

[19] X. Jehl, M. Sanquer, R. Calemczuk, and D. Mailly, Nature **405**, 50 (2000).

[20] A. A. Kozhevnikov, R. J. Schoelkopf, M. J. R. L. E. Calvet, and D. E. Prober, J. Low Temp. Phys. **118**, 671 (2000).

[21] F. Lefloch, C. Hoffmann, M. Sanquer, and D. Quirion, Phys. Rev. Lett. **90**, 067002 (2003).

[22] M. Büttiker, Phys. Rev. B **46**, 12485 (1992).

[23] W. D. Oliver, J. Kim, R. C. Liu, and Y. Yamamoto, Science **284**, 299 (1999).

[24] R. C. Liu, B. Odom, Y. Yamamoto, and S. Tarucha, Nature **391**, 263 (1998).

[25] R. Hanbury-Brown and R. Q. Twiss, Nature **177**, 27 (1956).

[26] M. Büttiker, *Quantum noise in mesoscopic physics*, Vol. 97 of *NATO science Series II: Mathmatics, Physics and chemistry* (Kluwer, Dordrecht, 2003), eds. Yuli. V. Nazarov,.

[27] P. Recher, E. Sukhorukov, and D. Loss, Phys. Rev. B **63**, 165314 (2001).

[28] Z. Yuan, B. Kardynal, R. Stevenson, A. Shields, K. C. C. Lobo, N. Beattie, D. Ritchie, and M. Pepper, Science **295**, 102 (2002).

[29] G. Burkard, D. Loss, and E. V. Sukhorukov, Phys. Rev. B **61**, R16303 (2000).

[30] G. Burkard and D. Loss, Phys. Rev. Lett. **91**, 087903 (2003).

[31] D. Loss and D. DiVicenzo, Phys. Rev. A **57**, 120 (1998).

[32] D. DiVicenzo and D. Loss, Superlattices and Microstructures **23**, 419 (1998).

[33] M.-S. Choi, C. Bruder, and D. Loss, Phys. Rev. B **61**, R16303 (2000).

[34] J. Torres, T. Martin, and G. B. Lesovik, Phys. Rev. B **63**, 134517 (2001).

[35] G. B. Lesovik, T. Martin, and G. Blatter, Eur. Phys. J. B **24**, 287 (2001).

[36] P. Recher and D. Loss, Phys. Rev. B **65**, 165327 (2001).

[37] C. Bena, S. Vishveshwara, L. Balents, and M. P. A. Fisher, Phys. Rev. Lett. **89**, 037901 (2002).

[38] N. M. Chtchelkatchev, G. Blatter, G. B. Lesovik, and T. Martin, Phys. Rev. B **66**, 161320(R) (2002).

[39] V. Bouchiat, N. Chtchelkatchev, D. Feinberg, G. B. Lesovik, T. Martin, and J. Torrès, Nanotechnology **14**, 77 (2003).

[40] P. Samuelsson and M. Büttiker, Phys. Rev. Lett **89**, 046601 (2002).

[41] P. Samuelsson and M. Büttiker, Phys. Rev. B **66**, R201306 (2002).

[42] D. Loss and E. V. Sukhorukov, Phys. Rev. Lett. **84**, 1035 (2000).

[43] J. B. Johnson, Phys. Rev. **29**, 367 (1927).

[44] H. Nyquist, Phys. Rev. **32**, 110 (1928).

[45] B. J. van Wees, H. van Houten, C. W. J. Beenakker, J. G. Williamson, L. P. Kouwenhoven, and D. van der Marel, Phys. Rev. Lett. **60**, 848 (1988).

[46] R. Landauer, IBM J. Res. Dev. **1**, 233 (1957).

[47] M. Büttiker, Y. Imry, R. Landauer, and S. Pinhas, Phys. Rev. B **31**, 6207 (1985).

[48] H. Birk, M. J. M. de Jong, and C. Schönenberger, Phys. Rev. Lett. **75**, 1610 (1995).

[49] M. J. M. de Jong and C. W. J. Beenakker, *Mesoscopic Electron Transport*, Vol. 345 of *NATO Advanced Studies Institute, Series E: Applied Sciences* (Kluwer, Dordrecht, 1997), p. 44, eds. L. L. Sohn, L. P. Kouwenhoven and G. Schön.

[50] A. A. Andreev, Sov. Phys. JETP **19**, 1228 (1964).

[51] M. J. M. de Jong and C. W. J. Beenakker, Phys. Rev. B **49**, 16070 (1994).

[52] G. E. Blonder, M. Tinkham, and T. M. Klapwijk, Phys. Rev. B **25**, 4515 (1982).

[53] J. C. Cuevas, A. Martin-Rodero, and A. Levi Yeyati, Phys. Rev. B **54**, 7366 (1996).

[54] H. Courtois, P. Charlat, D. M. Ph. Gandit, and B. Pannetier, J. Low Temp. Phys. **116**, 187 (1999).

[55] H. Courtois, P. Gandit, D. Mailly, and B. Pannetier, Phys. Rev. Lett. **76**, 130 (1996).

[56] C. W. J. Beenakker, Phys. Rev. B **46**, 12841 (1992).

[57] V. A. Khlus, Sov. Phys. JETP **66**, 1243 (1987).

[58] R. Hanbury-Brown and R. Q. Twiss, Nature **178**, 1447 (1956).

[59] M. P. Anantram and D. Supriyo, Phys. Rev. B **53**, 16390 (1996).

[60] T. Martin, Phys. Lett. A **220**, 137 (1996).

[61] J. Torres and T. Martin, Eur. Phys. J. B **12**, 319 (1999).

[62] J. Börlin, W. Belzig, and C. Bruder, Phys. Rev. Lett **88**, 197001 (2002).

[63] P. Recher and D. Loss, Phys. Rev. Lett. **91**, 267003 (2003).

[64] C. W. J. Beenakker and H. van Houten, *Quantum transport in semiconductor nanostructures*, Vol. 44 of *Solid state physics* (Academic Press, San Diego, 1991), eds. H. Ehreneich, D. Turnbull.

[65] Y.-C. Shih, M. Murakami, E. Wilkie, and A. Callegari, J. Appl. Phys **62**, 582 (1987).

[66] M. Murakami, K. Childs, J. Baker, and A. Callegari, J. Vac. Sci. Technol. B **4**, 903 (1986).

[67] Private communcation with T. Akazaki, and H. Takyanagi.

[68] P. Dubos, P. Charlat, T. Crozes, P. Paniez, and B. Pannetier, J. Vac. Sci. Technol. B **18**, 122 (2000).

[69] Y. Harada, D. B. Haviland, P. Delsing, C. Chen, and T. Claeson, Appl. Phys. Lett. **65**, 636 (1994).

[70] N. W. Ashcroft and N. D. Mermin, *Solid state physics* (Saunders College Publishing, Florida, 1976).

[71] T. Hoss, C. Strunk, T. Nussbaumer, R. Huber, U. Staufer, and C. Schönenberger, Phys. Rev. B **62**, 4079 (2000).

[72] L. J. van der Pauw, Philips Res. repts. **13**, 1 (1958).

[73] K. v. Klitzing, G. Dorda, and M. Pepper, Phys. Rev. Lett. **45**, 494 (1980).

[74] S. Datta, *Electronic Transport in Mesoscopic Systems* (Cambridge University Press, Cambridge, 1995).

[75] F. Pobell, *Matter and methodes at low temperatures* (Springer-Verlag, Berlin, 1996), - 2nd ed.

[76] D. C. Glattli, P. Jacques, P. P. A. Kumar, and L. Saminadayar, J. Appl. Phys. **81**, 7350 (1997).

[77] T. Gramespacher and M. Büttiker, Phys. Rev. B **61**, 8125 (2000).

[78] A. Kumar, L. Saminadayar, D. C. Glattli, Y. Jin, and B. Etienne, Phys. Rev. Lett. **76**, 2778 (1996).

[79] M. Reznikov, M. Heiblum, H. Shtrikman, and D. Mahalu, Nature **399**, 238 (1999).

[80] G. B. Lesovik, JETP-Letters **49**, 592 (1989).

[81] M. Büttiker, Phys. Rev. Lett. **65**, 2901 (1990).

[82] Y. M. Blanter and E. V. Sukhorukov, Phys. Rev. Lett. **84**, 1280 (2000).

[83] Y. M. Blanter and M. Büttiker, Phys. Rep. **336**, 1 (2000).

[84] D. Averin and H. T. Imam, Phys. Rev. Lett. **76**, 3814 (1996).

[85] K. Nagaev and M. Büttiker, Phys. Rev. B **63**, R081301 (2001).

[86] P. Roche, H. Perrin, D. C. Glattli, H. Takayanagi, and T. Akazaki, Physica C **352**, 73 (2001).

[87] C. Hoffmann, F. Lefloch, and M. Sanquer, Eur. Phys. J. B. **29**, 629 (2002).

[88] B. A. Muzykantskii and Khmelnitskii, Phys. Rev. B **50**, 3982 (1994).

[89] M. Büttiker and P. Samuelsson, Physica E **18**, 60 (2003).

[90] J. Nitta, T. Akazaki, and H. Takyanagi, Phys. Rev. B **46**, R14286 (1992).

[91] K. Neurohr, A. A. Golubov, T. Klocke, J. Kaufmann, T. Schäpers, J. A. D. Uhlisch, A. V. Ustinov, M. Hollfelder, H. Lüth, and A. I. Braginski, Phys. Rev. B **54**, 17018 (1996).

[92] Y. Takagaki, Phys. Rev. B **57**, 4009 (1996).

[93] E. Toyoda, T. Akazaki, and H. Takyanagi, Phys. Rev. B **59**, R11653 (1999).

[94] Y. Imry, *Introduction to mesoscopic physics* (Oxford University Press, Oxford, 1997).

[95] C. W. J. Beenakker, B. Rejaei, and J. A. Melsen, Phys. Rev. Lett. **72**, 2470 (1994).

[96] W. Belzig, A. Brataas, Y. V. Nazarov, and E. W. Bauer, Phys. Rev. B **62**, 9726 (2000).

[97] M. Jakob, H. Stahl, J. Knoch, J. Appenzeller, B. Lengeler, H. Hardtdegen, and H. Lüth, Appl. Phys. Lett. **76**, 1152 (2000).

[98] M. L. Roukes, M. R. Freeman, R. S. Germain, R. C. Richardson, and M. B. Ketchen, Phys. Rev. Lett. **55**, 422 (1985).

[99] C. Wellstood, F. C. Urbina and J. Clake, Phys. Rev. B **49**, 5942 (1985).

[100] K. E. Nagaev, Phys. Rev. B **52**, 4740 (1995).

[101] M. Henny, H. Birk, R. Huber, C. Strunk, A. Bachtold, M. Krüger, and C. Schönenberger, Appl. Phys. Lett. **71**, 773 (1999).

[102] K. Harada, O. Kogure, Murase, and Kei, IEEE J. Solid-state circuit **SC-17**, 148 (1982).

[103] K. Harada, IEEE Tran. Electron Devices **ED-29**, 518 (1982).

# *Curriculum Vitae*

Bong-Ryoul Choi

| | |
|---|---|
| 19. 12. 1970 | Born in Jeonju, Jeonbuk, Korea (R.O.K.) |
| 1994 - 1998 | Undergraduate study in Physics department, Chonbuk national university, Jeonju, Korea |
| 1998 | Bachelor of Science in Physics on the subject "Quantum interference effect in mesoscpic system" under the supervisor Prof. Dr. J.-J. Kim in Physics department, Chonbuk national university, Jeonju, Korea |
| 1998 - 2000 | Master study in the international master program in Physics and engineering physics, Chalmers university of technology, Gothenberg, Sweden. |
| 2000 | Master of science in Physics on the subject "Normal metal hot-electron microbolometer with capacitive coupling to the antenna by tunnel junctions" under the supervisor Prof. Dr. Leonid Kuzmin in Physics and engineering physics, Chalmers university of technology, Gothenberg, Sweden. |
| 2000 - 2004 | Ph.D. work under the supervisor Prof. Dr. Christian Schönenberger on the subject "Quantum shot noise in superconductor-semiconductor heterostructures" at institute of Physics, University of Basel, Basel, Switzerland |
| 01. 10. 2004 | Thesis defence |

**Folgenden Dozentinnen und Dozenten verdanke ich meine wissenschaftliche Ausbildung:**

J.-H. Kim, J.-J. Kim, J.-S. Kim, C. Park, J.-M. Seo, D.-S. Soh, L.-I. Lee, J.-K. Lee, C.-H. Lim, Y.-H. Lee, H.-J. Lee, J.-Y. Kim, G. Wendin, J. Kinaret, M. Jonson, L. Kuzmin, T. Claeson, V. Shumeiko, P. Samuelsson, R. Ryberg, G. Wahnström, C. Schönenberger, W. Belzig, Y. Yamamoto.